

General Disclaimer

One or more of the Following Statements may affect this Document

- This document has been reproduced from the best copy furnished by the organizational source. It is being released in the interest of making available as much information as possible.
- This document may contain data, which exceeds the sheet parameters. It was furnished in this condition by the organizational source and is the best copy available.
- This document may contain tone-on-tone or color graphs, charts and/or pictures, which have been reproduced in black and white.
- This document is paginated as submitted by the original source.
- Portions of this document are not fully legible due to the historical nature of some of the material. However, it is the best reproduction available from the original submission.

DOE/JPL/956312--08

Distribution Category UC-63

**Mobil Solar Energy Corporation
16 Hickory Drive
Waltham, Massachusetts 02254**

DOE/JPL/956312--08

DE85 001707

STRESS STUDIES IN EFG

Program Manager: Juris P. Kalejs

Quarterly Progress Report - Subcontract No. 956312

Covering Period: April 1, 1984 to June 30, 1984

Distribution Date: August 15, 1984

"The JPL Flat Plate Solar Array Project is sponsored by the U.S. Department of Energy and forms part of the Solar Photovoltaic Conversion Program to initiate a major effort toward the development of flat plate solar arrays. This work was performed for the Jet Propulsion Laboratory, California Institute of Technology by agreement between NASA and DOE."

ABSTRACT

Electrical characterization of defects induced in FZ and CZ silicon stress in four-point bending above 1200°C has been started. Techniques to study electrical activity that will permit correlation of defect activity with diffusion length and with room and low temperature EBIC are being developed.

Preliminary characterization of defects in ribbon grown at very low speeds of less than 1 cm/min shows that the dislocation density is very low over significant regions of cross section, while regions of high dislocation density ($\sim 5 \times 10^6/\text{cm}^2$) occur in bands in a number of places.

Additional measurements of stress distributions in EFG material have been obtained at the University of Illinois using shadow-Moire interferometry.

"This report was prepared as an account of work sponsored by the United States Government. Neither the United States nor the United States Department of Energy, nor any of their employees, nor any of their contractors, subcontractors, or their employees, makes any warranty express or implied, or assumes any legal liability or responsibility for the accuracy, completeness or usefulness of any information, apparatus, product or process disclosed, or represents that its use would not infringe privately owned rights."

TABLE OF CONTENTS

<u>SECTION</u>		<u>PAGE</u>
	ABSTRACT	iii
I	INTRODUCTION	1
II	PROGRESS REPORT	3
	A. Advanced System Design	3
	1. Experimental	3
	2. Theoretical	7
	3. Results	10
	B. EFG Defect Electrical Characterization	22
	1. Introduction	22
	2. Sample Preparation	23
	3. Preparation of Schottky Barriers and Back Contacts	25
	4. EBIC Analysis	26
	5. Diffusion Length Measurements	26
	6. Results	27
	C. Creep Law Studies	34
	D. Residual Stress Measurements	34
	REFERENCES	34
	APPENDICES	35

TABLE OF CONTENTS (continued)

List of Figures

FIGURE

1	Schematic of EFG test system	4
2	EFG ribbon growr at 0.8-0.9 cm/min	6
3	Schematic diagram of the EFG system and estimated temperatures of the tilt shield and the insulation blocks ...	8
4	Stress distribution along the axis of the sheet	11
5	Stress distribution along the width of the sheet	12
6	Temperature distribution of the surroundings and the sheet centerline	15
7	Operating curves of variations in the sheet thickness for new system as a function of the pull rate	17
8	(A) Effect of dimensions of the capillary spacing and die flats and length of the viewing slot on the sheet thickness for new system at capillary spacing; (B) Asymmetric environment temperature distribution; (C) Dependence of the sheet thickness on the static head	19
9	Variations in (A) shapes of the melt/solid interface, and (B) aluminum profiles at growth rates of 2 and 1 cm/min	21
10	Beam induced specimen current vs. beam current for a CZ solar cell	24
11	Low temperature EBIC micrographs	29
12	Room temperature and low temperature EBIC of same region for stressed carbon-rich CZ	30
13	High magnification EBIC micrographs of dislocations	32
14	Contrast profile of line scan shown in Fig. 13	33

I. INTRODUCTION

A satisfactory model that can account for stresses generated in silicon sheet grown at high speeds is not yet available. Many attempts to calculate residual stresses have been made, but all of these suffer from inadequacies in one area or another. This report describes the work in progress under this subcontract to attempt to develop and test in the laboratory a stress-temperature field model for silicon ribbon EFG. In one subtask, a computer code developed at Harvard University to calculate stress with plastic deformation in steady-state sheet growth is being applied to study temperature field-stress relationships. The stress state is parameterized by a two-dimensional temperature field and growth speed. Incorporation of time dependent stress relaxation effects is through a creep law to model the impact of plastic flow on the sheet residual stress state. A second aspect of the program deals with the development of a model to predict the temperature field in a moving sheet from given system component temperatures (i.e., the sheet environment), and studies experimental means to verify the model. This work is attempting to integrate temperature field modeling in the solid which takes into account real system geometries with a more detailed heat transfer model developed at MIT for the die top and meniscus regions below the growth interface.

The predictions of the stress analysis and temperature field models are supported on a qualitative level by experimental results obtained from characterization of 10 cm wide ribbon grown in an EFG cartridge system. Residual stresses in both buckled and unbuckled as-grown ribbon are much lower than predicted for the thermoelastic case. These can only be achieved through high rates of creep for the temperature profiles that are calculated for the 10 cm ribbon. Defects are observed in the ribbon cross section which originate from strain instabilities.

Both modeling and experimental work are in progress to attempt to apply the stress analysis at a more quantitative level. The modeling is examining stress-temperature field relationships in a search for low stress growth configurations. The experimental efforts are in study of the high temperature creep response of silicon to provide information on the constitutive relationship, development of a technique to measure the temperature field in the sheet during growth, and of means to measure residual stress distributions. A temperature sensor based on fiber optics has been constructed for the temperature field measurements. A laser interferometry technique is being evaluated for residual stress measurements at the University of Illinois.

Attempts to verify aspects of the stress and temperature field modeling with the 10 cm cartridge system have met with limited success. Due to the complexity of the growth interface environment it has not been possible to use the fiber optics sensor. The cartridge system has lacked flexibility to allow imposition of changes in growth conditions and system temperature fields in a known and controllable manner in order to study temperature field-stress relationships at a quantitative level. A system that has the required flexibility for testing of the stress analysis model is being constructed.

II. PROGRESS REPORT

A new subtask has been started to develop techniques to measure defect electrical activity using the EBIC mode of the scanning electron microscope both at low ($\sim 80^{\circ}\text{K}$) and high (room) temperatures (see Section B below).

The stress modeling task has focused on examination of a new EFG growth configuration which will be used to test the model. Growth has been established at speeds of the order of 1 cm/min for 5 cm wide ribbon. Initial characterization of ribbon grown at low speeds shows that dislocation densities are low in comparison to those typical of 10 cm wide ribbon (see Section A below).

A. Advanced System Design

1. Experimental

Attempts to grow 5 cm wide ribbon in the new design of system in Furnace 17 have been successful. A schematic of the growth configuration is given in Fig. 1. There have been a number of changes made from the cartridge mode of growth in order to simplify the thermal environment of the sheet above the growth interface. This allows more straightforward thermal and stress analysis to be performed and also gives flexibility to change the post-solidification cooling profile through adjustments of insulation.

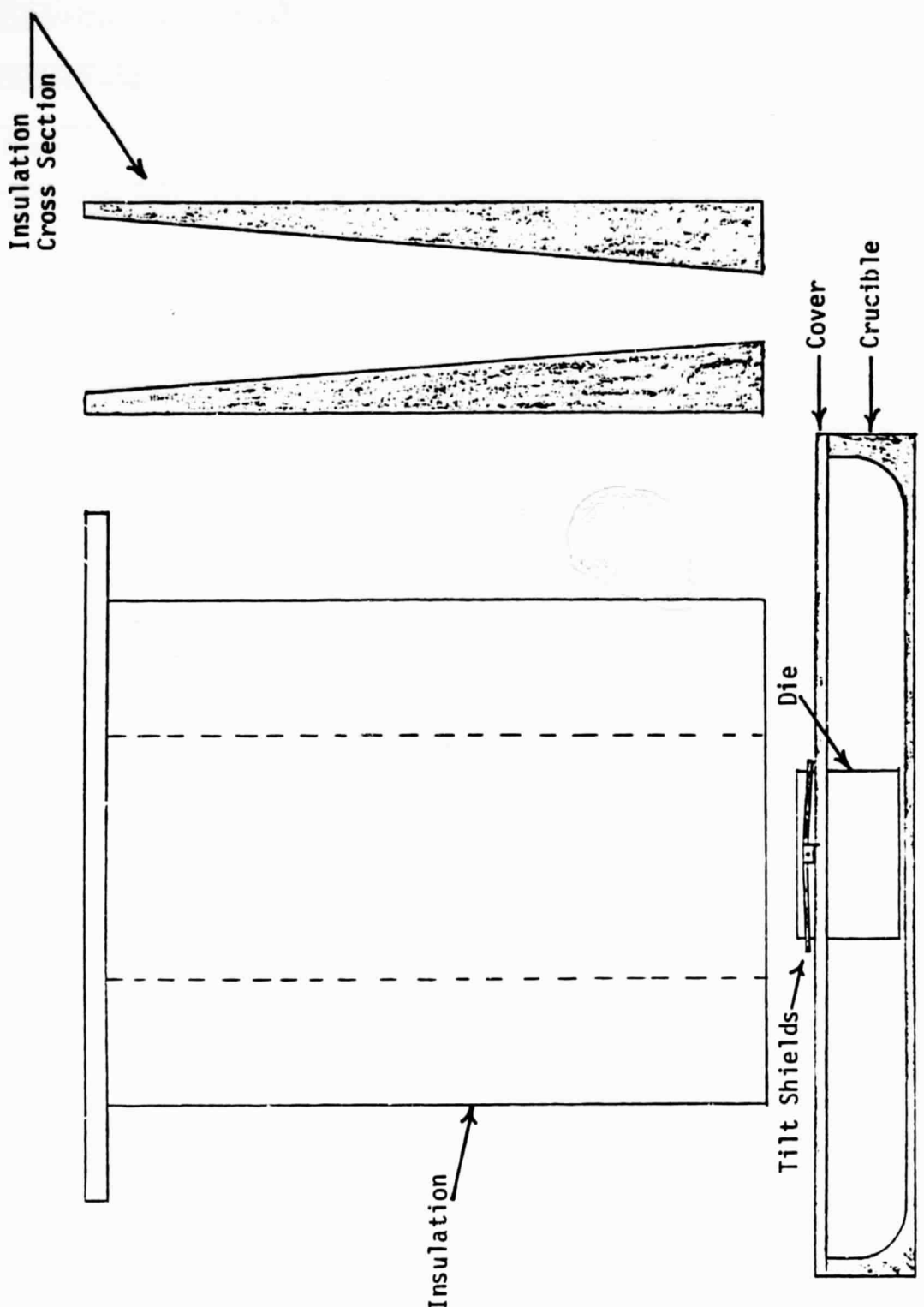


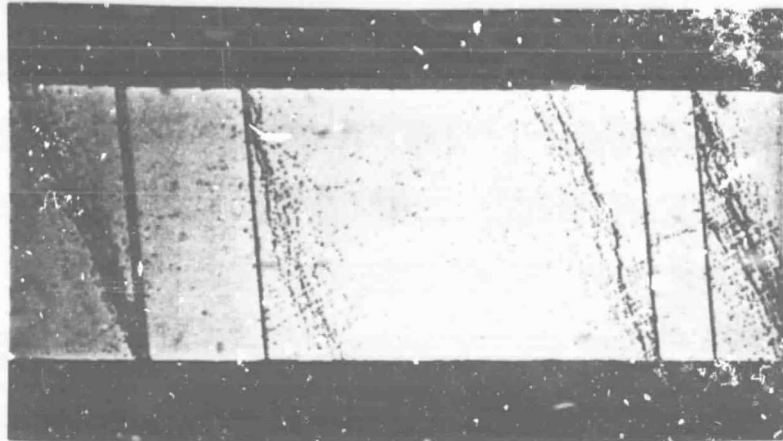
Fig. 1. Schematic of EFG test system.

An additional feature of the system shown in Fig. 1 is that the die is very short, lowering h_{eff} and thus providing more flexibility to choose growth conditions. Growth is established through ramping of the main zone heater, which is the only active heater in this system.

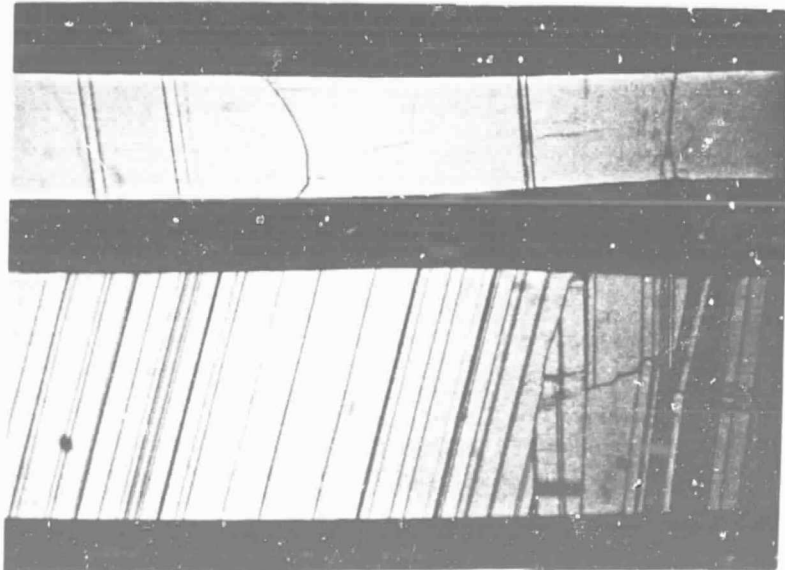
The main problems to overcome in the initial trials were establishment of a means to balance ribbon edge temperature gradients, and of a technique to ramp the main zone to compensate for latent heat generation while the growth speed was being attained. The former was accomplished by installation of movable radiation, or "tilt" shields at die top level. The ramping of the main zone to establish growth was found to be manageable. The transients are much slower than those customarily found in the cartridge system, but accommodation can be made easily by adjusting the ramp rate. This is done manually at present.

Cross-sectional micrographs have been prepared of ribbon grown at speeds below 1 cm/min. Representative photographs are given in Fig. 2. In general, there are large areas of the order of 1 cm in extent that have low dislocation densities, such as in Fig. 2(b). When higher dislocation regions are found, they appear to be confined to certain grains and often appear as bands of the type that may be associated with Lüders strain. Such a region is shown in Fig. 2(a).

Dislocation counts have been made in a number of representative regions. These range from about $5 \times 10^5/\text{cm}^2$ to as high as $7 \times 10^6/\text{cm}^2$ in the higher dislocation bands, to zero over grains that cover a significant portion of the cross section. Other ribbon will be grown and examined to establish characteristics of the defect structure typical of this growth mode.



(a)



(b)

Fig. 2. EFG ribbon grown at 0.8-0.9 cm/min: (a) high magnification dislocated region of Lüders bands (thickness 0.23 mm); (b) low magnification dislocation-free regions of thin (0.36 mm) and thick (0.75 mm) ribbon.

2. Theoretical (H.M. Ettouney)

a. Introduction

Residual (room temperature) stresses in silicon sheets have a direct effect on the final yield of the product material. Large residual stresses result in a product material with low strength which tends to crack and split during subsequent processing steps, e.g., cutting and cell manufacturing.

The studies presented here are focused on understanding the dependence of the room temperature stresses on operating variables, e.g., pull rate and static head, and on the heat transfer configuration, e.g., location and length of cooling and heating elements and die dimensions. The study is pursued through the use of detailed finite element models of plane stress [1] and heat and mass transfer [2,3] to simulate the field variables in an EFG configuration that has been constructed for the purpose of testing the stress analysis model.

The EFG system modeled (see Fig. 3) has a simpler heat transfer configuration than the standard cartridge system [4]. Therefore, the number of system parameters that have to be varied in order to control the growth process are reduced to temperature of the main zone, which indicates the amount of input heat to the crucible; location and position of the tilt shields which have a direct effect on controlling the rate of heat transfer to the surroundings in the meniscus region; and the pull rate. The full definition of the heat transfer environment will also depend on dimensions of the die, i.e., lengths of the capillary spacing (l_1) and the die flats (l_2), and thickness,

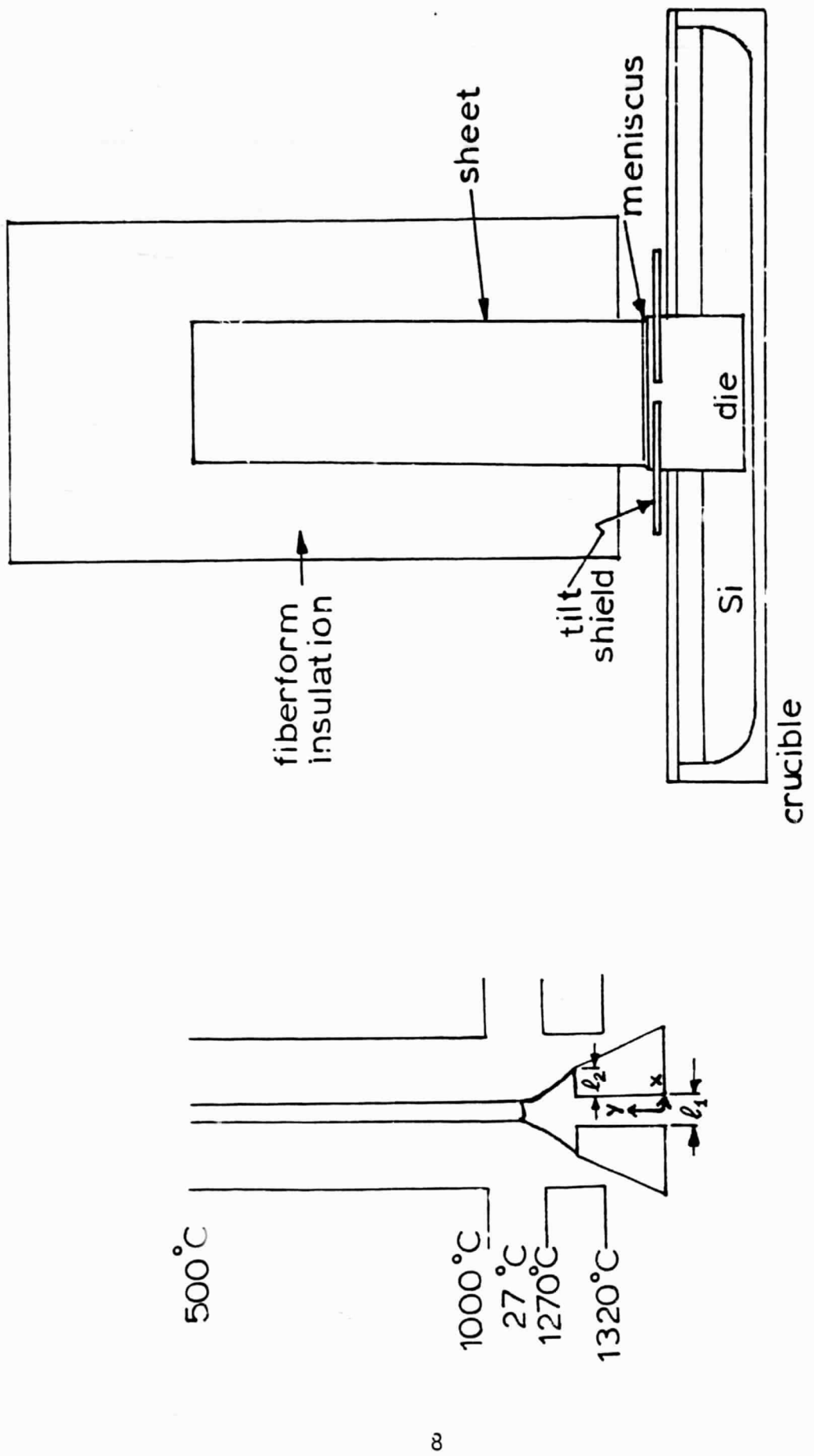


Fig. 3. Schematic diagram of the EFG system and estimated temperatures of the tilt shield and the insulation blocks.

position, and type of the insulation. This is a less complicated set of parameters than considered in the finite element simulation of the cartridge system [3].

The first part of this study is focused on reporting the finite element results for the simulation of plane stresses, heat transfer, and dopant distribution. In the second part, experimental measurements are presented for the variation in residual stress, sheet thickness, and dopant segregation as a function of the operating conditions. In addition, experimental observation of thermal operating limits will be discussed and also compared to the finite element calculations. To establish a basis for the finite element calculations of this EFG configuration, which are presented in the next section, some of the finite element results for simulating the cartridge system [3] are presented and discussed in parallel.

The results section is divided into four parts. In the first, the stress results are presented; in the second part, the operating diagram of the new system is constructed; in the third part, sensitivity of the system is discussed with respect to variations in the die dimensions, thermal asymmetry, and the static head; and in the fourth part, aluminum profiles and its segregation along the melt/solid interface are presented for representative operating points. In order to facilitate reading of the results, it is important to mention that in all of the calculations for this system the following parameters were used, unless otherwise mentioned: a growth rate of 2 cm/min, die temperature of 1747^0K , capillary spacing (l_1) of 0.0254 cm, die flats (l_2) of 0.0254 cm, symmetric temperature profile for the surroundings

(see Fig. 3), and the physical properties given in [2]. Also, the dimensionless temperature is scaled by a reference temperature of 1783°K and the dimensionless length is scaled by a reference length of 0.025 cm.

3. Results

a. Stress Calculations

The stress distribution in the silicon sheet is intimately affected by the heat transfer configuration, the axial temperature distribution in the sheet, and the form of the creep law. All of these factors affect the rate of strain, especially close to the melt/solid interface, which in turn dictates the final magnitude of the residual stress. In the following results, the high creep law (see Ref. [1]) was used to calculate the stresses. Figures 4(a) and 5(a) show the stress distribution along the sheet centerline and edge, respectively, for the cartridge system. These profiles are calculated at growth rates of 3 and 4 cm/min and for the operating conditions obtained for the theoretical fit of the variations in the sheet thickness as a function of the pull rate to the experimentally measured data [3]. As is shown, the behavior of the system reproduces the predictions of Ref. [1].

To present the stress distribution in the new EFG configuration, a range of operating conditions is examined which includes the die dimensions, the heat transfer configuration, the pull rate, the die temperature, and the static head. The stress profiles shown in Figs. 4(b) and 5(b) are calculated at the operating conditions of curve b in Fig. 8(b) and they are typical of the heat transfer configuration used

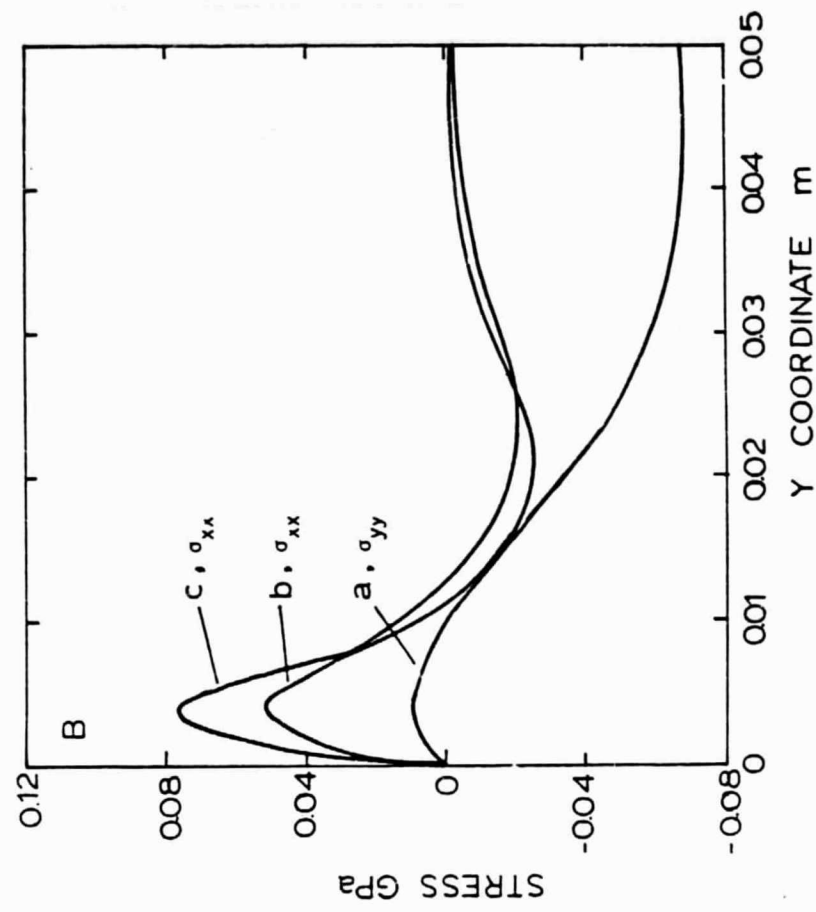
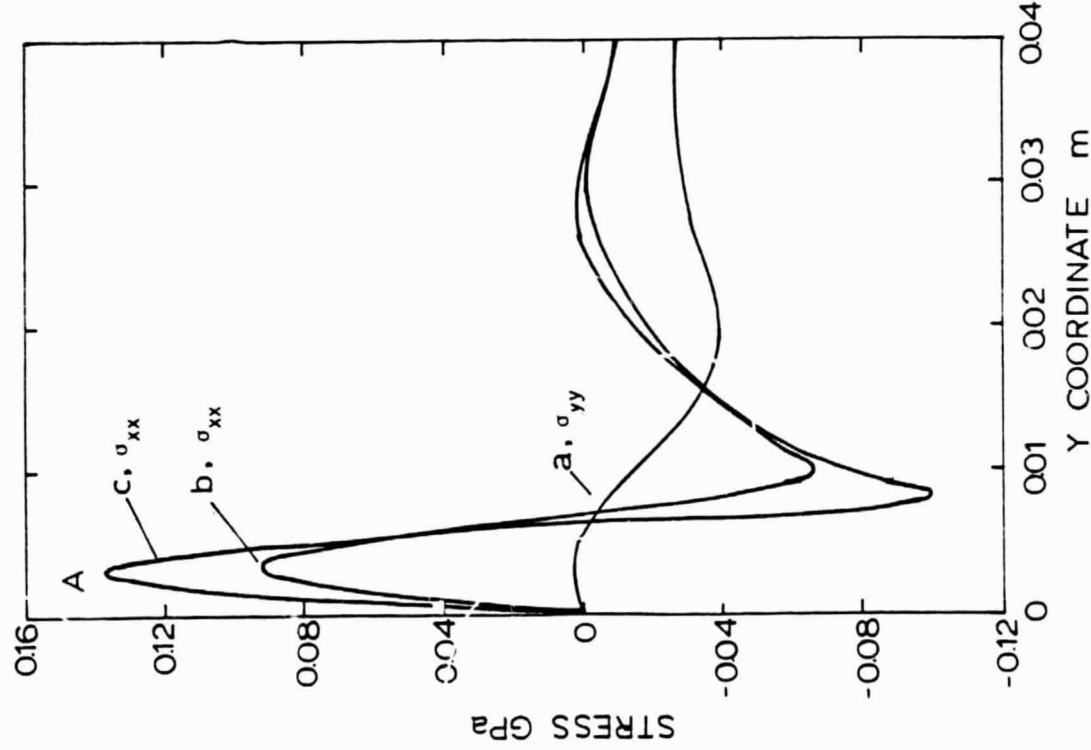


Fig. 4. Stress distribution along the axis of the sheet for: (A) The cartridge system at growth rates of (a,b) 3 cm/min, and (c) 4 cm/min. The rest of the operating conditions are given in [3]. (B) The EFG system at a growth rate of 2 cm/min and static heads of (a,b) 2 cm, and (c) 4 cm. The rest of the operating conditions are those of curve c in Fig. 7.

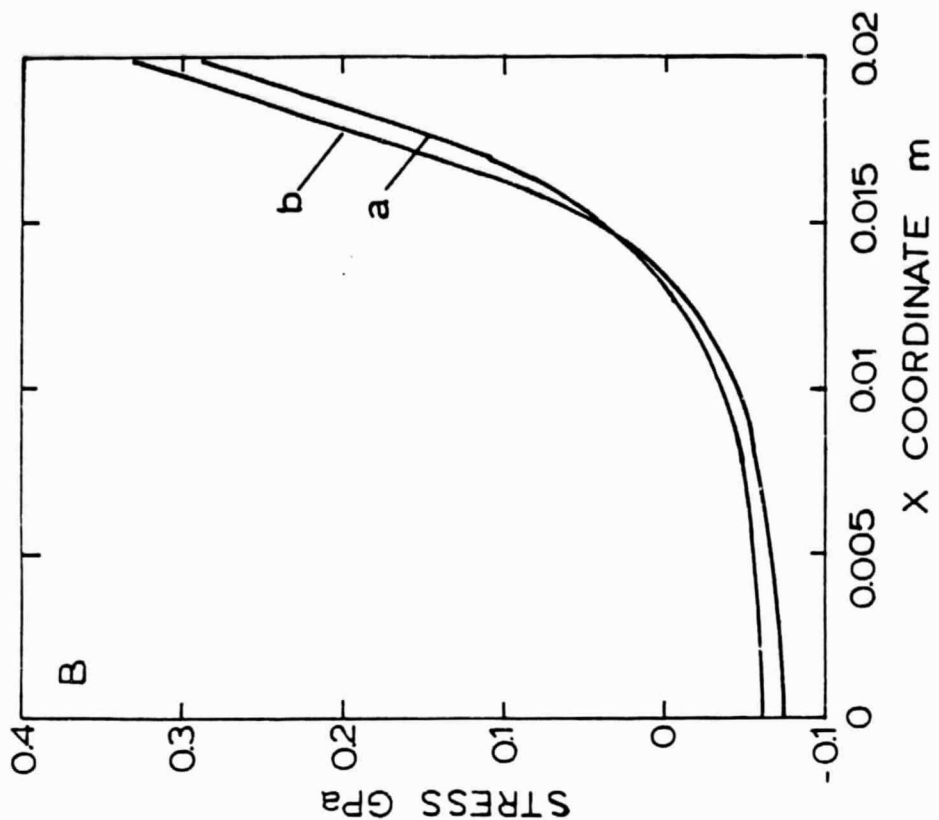
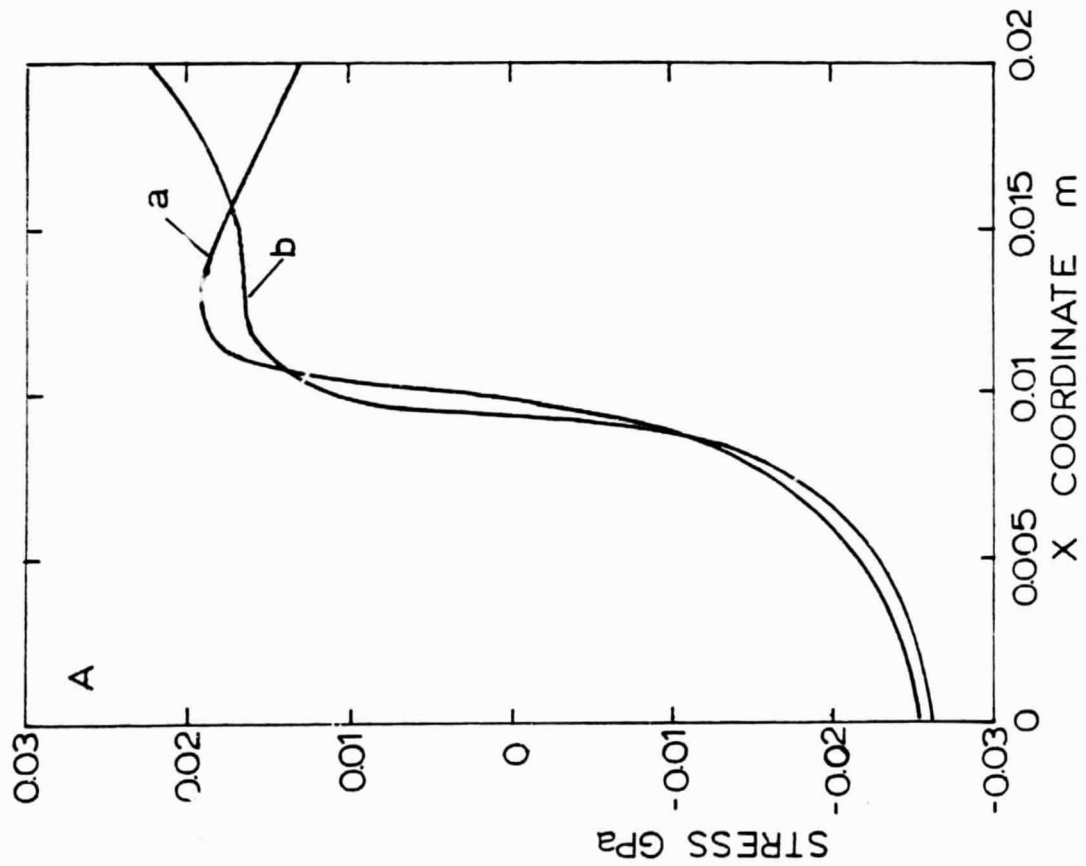


Fig. 5. Stress distribution (σ_{xy}) along the width of the sheet for (A) the cartridge system at growth rates of (a) 3 cm/min and (b) 4 cm/min, and for (B) the EFG system at growth rate of 2 cm/min and static heads of (a) 2 cm and (b) 3 cm. The rest of the operating conditions for both system are the same as in Fig. 4.

to simulate the new EFG system; examine Table I which includes values of residual stress and maximum radial stress as a function of system parameters and operating conditions. As is shown, larger residual stresses are calculated at the edge of the sheet for this system than for the cartridge. The shape of the temperature profiles of the surroundings and of the silicon sheet are responsible for the increase in the magnitude of residual stresses. These are displayed in Figs. 6(a) and (b). The high temperature reheat region in the cartridge system allows the material to creep and as a result axial stresses level off instead of increasing, as in the new system. In addition, with inspection of Table I one can see that lowering of residual stresses by lowering the pull rate and the die temperature (which reduces the amount of input heat into the system and in turn the temperature gradient in the solid phase) is restricted by operation limits. First, reduction of the pull rate at a constant sheet thickness is associated with increase in the die temperature; this in turn increases the temperature gradient in the solid phase and as is shown in Table I, which offsets the effect of decreasing the pull rate. Second, reduction of the pull rate at constant die temperature is limited by melt freezing at the die top at low die temperatures, while at higher die temperatures larger temperature gradients are present because the sheet gets thinner.

b. Sheet Thickness, Growth Rate, Die Temperature
Operating Diagram

Development of the operating curves in the t - V_s - T_0 space is very important since it predicts the course of operation,

Table I. Variations in the sheet thickness (t), meniscus height (s), contact angle (θ_c), interface temperature gradients (G_L and G_s), residual stress (σ_{yy}), and maximum transverse stress (σ_{xx}) as a function of the die temperature (T_o), and the growth rate (v_s).

Static Head = 2 cm.

Capillary Length = Length of die flat (l_2) = 0.0254 cm.

v_s (cm/min)	t (cm)	s (cm)	θ_c	G_L (0 K/cm)	G_s (0 K/cm)	σ_{xx} (GPa)	σ_{yy} (GPa)
Die Temperature = 1774^0 K							
0	0.0524	0.0360	65	501	1463	-	-
0.2	0.0385	0.0489	60	566	1731	0.0473	0.191
0.4	0.0235	0.0602	56	720	2281	0.0712	0.232
Die Temperature = 1765^0 K							
0	0.0710	0.0110	75	437	1261	-	-
1	0.0270	0.0570	56	593	2083	0.0745	0.268
1.5	0.0097	0.0687	52	986	3631	0.0134	0.311
Die Temperature = 1756^0 K							
0.5	0.0683	0.0156	73	380	1261	-	-
1	0.0490	0.0393	64	397	1483		
2	0.0190	0.0630	54	610	2479		
2.5	0.0123	0.0672	52	753	3137		
Die Temperature = 1747^0 K							
1	0.0656	0.0199	71	326	1268	0.0436	0.216
2	0.0342	0.0523	58	388	1784	0.0684	0.282
3	0.0173	0.0641	54	532	2563	0.1010	0.336
3.5	0.0132	0.0666	53	608	2984	0.1215	0.358
Die Temperature = 1738^0 K							
1.3	0.0691	0.0144	74	279	1226	-	-
2	0.0470	0.0406	64	283	1472		
3	0.0276	0.0572	57	346	1985		
4	0.0167	0.0645	54	434	2582		
Die Temperature = 1729^0 K							
1.8	0.0667	0.0181	72	224	1231	-	-
2	0.0610	0.0261	69	220	1286		
3	0.0374	0.0490	59	240	1666		
4.5	0.0195	0.0620	54	305	2345		

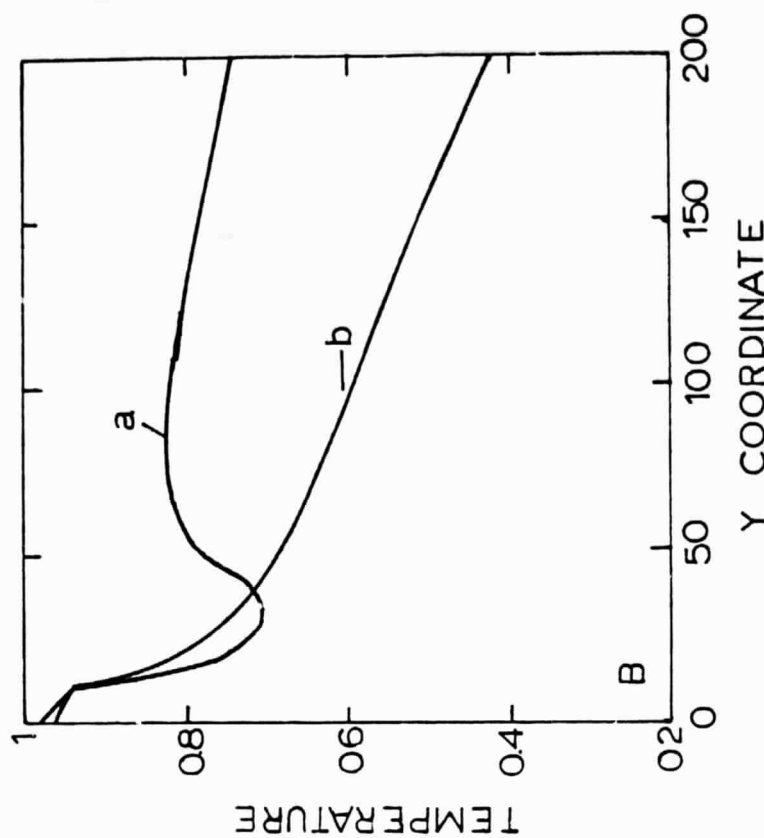
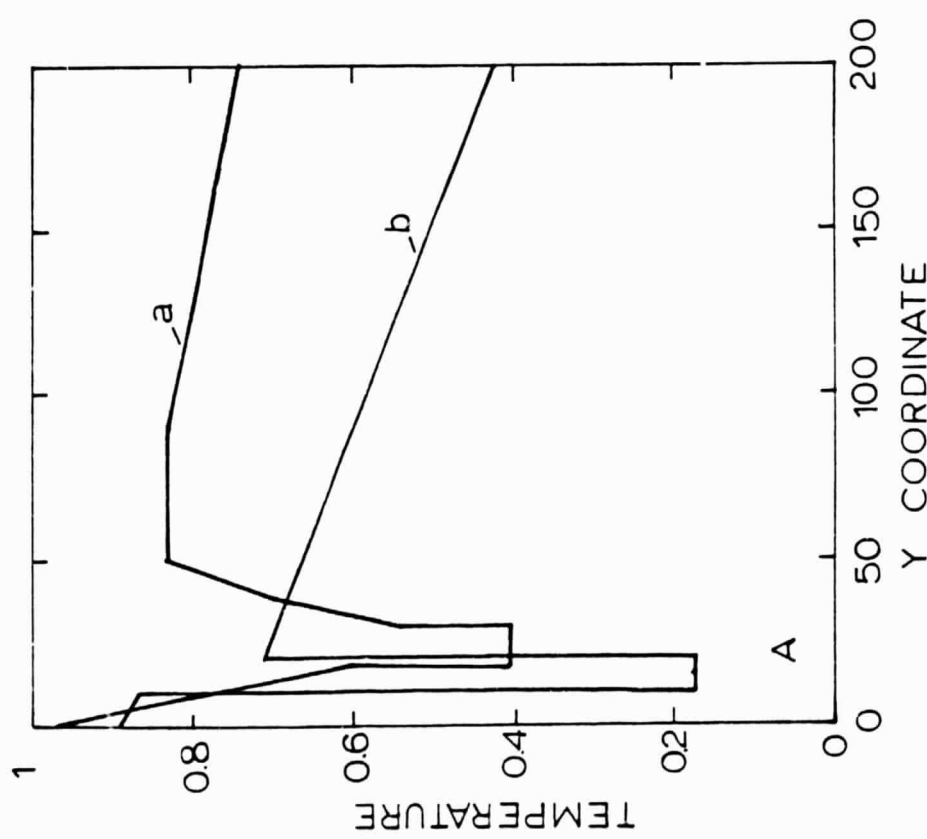


Fig. 6. Temperature distribution of (A) the surroundings, and (B) the sheet centerline for (a) the cartridge system, and (b) the new EFG configuration. The temperature and coordinate are dimensionless and scaled to 1783K and 0.025 cm, respectively.

which starts with seeding, where $V_g = 0$, followed by simultaneous increase in the pull rate and decrease in the die temperature (in this experiment, the main zone), respectively, in order to keep the sheet thickness constant, which is done experimentally by maintaining the meniscus at constant height. The operating curves for the EFG system, displayed in Fig. 7, are calculated at equal capillary spacing and die flats of 0.0254 cm, static head of 2 cm, and the surrounding temperature profile shown in Fig. 6(A), curve b. Upon constructing Fig. 7, attention has been paid to obtain theoretical data around the growth rate of 2 cm/min which is expected to be an average value for the experiments. This value is based on initial experimental results. An important aspect which should be mentioned is that the contact angle at the die edge for all the operating curves shown in Fig. 7 remains far from both of Gibb's limits. This can be attributed to the fact that the operating static head is relatively low. The average slope of the operating curves in Fig. 7, which can be used to describe the system sensitivity with respect to variations in the growth rate, is -0.033 s^{-1} , compared to an average slope of 0.011 s^{-1} calculated for the cartridge system [3]. The increase in the system sensitivity in the $t-V_g-T_0$ space is due to the increase of the edge-to-edge distance at the die top and total thermal mass of the system.

c. Sensitivity with Respect to Variations in Die Dimensions and Surrounding Temperature

Once the appropriate operating parameters are established, the operating diagram can be used to study the sensitivity of the growth process with respect to variations in the system

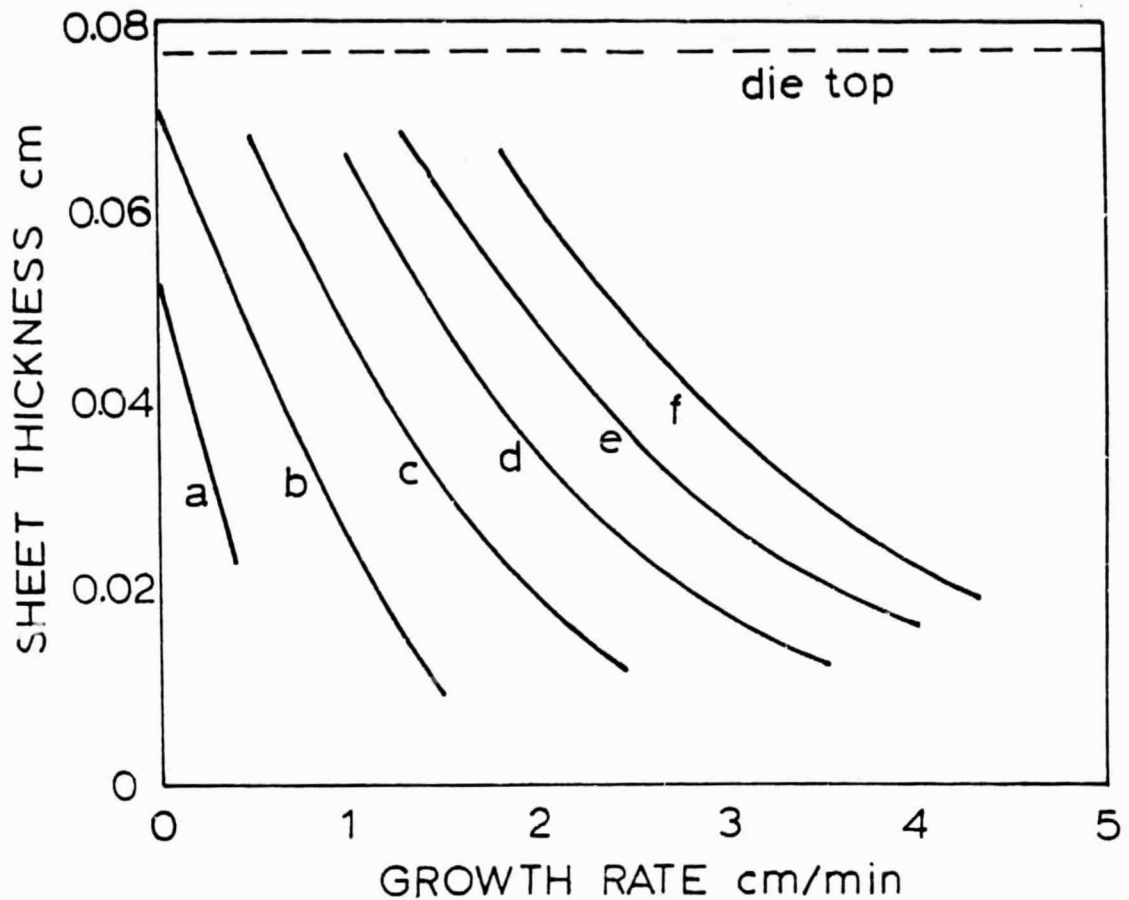


Fig. 7. Operating curves of variations in the sheet thickness for new system as a function of the pull rate at die temperatures of (a) 1774^0K , (b) 1765^0K , (c) 1756^0K , (d) 1747^0K , (e) 1738^0K , and (f) 1730^0K ; capillary spacing (l_1) is 0.0254 cm, die flat (l_2) is 0.0254 cm, and static head is 2 cm.

parameters. This aids in choosing a set of parameters to design a system with the lowest possible sensitivity towards variations in the operating conditions. The two system parameters considered in the following calculations are the die dimensions, lengths of the capillary spacing and die flats, and the environment temperature. Figure 8(a) shows the change in the sheet thickness as the capillary spacing (l_2) is increased from 0.0254 cm to 0.0662 cm, keeping the edge-to-edge distance constant, as a function of the length of viewing window. It is clear that replacing the die material with molten silicon resulted in increasing the thermal mass of the system, the meniscus height, and the sheet thickness. However, the overall sensitivity of the system did not change since the net amount of heat into the system is kept constant. The increase in the sheet thickness as the length of the viewing window is increased occurs because of the increase in the rate of heat transfer to the surroundings.

In the second test case, the thermal symmetry of the system is eliminated by pulling out one side of the insulation blocks. At these conditions, it is expected that the environment has a lower effective temperature because of its lower thermal capacity. Therefore, the net result is that the silicon sheet radiates to a background of lower temperature distribution on one side (see Fig. 8(b)). The finite element results for these conditions are displayed in Fig. 8(c). As is shown, sensitivity variations are also limited since radiation to the surroundings is only a secondary effect - the heat transfer process, which is still dominated by conduction.

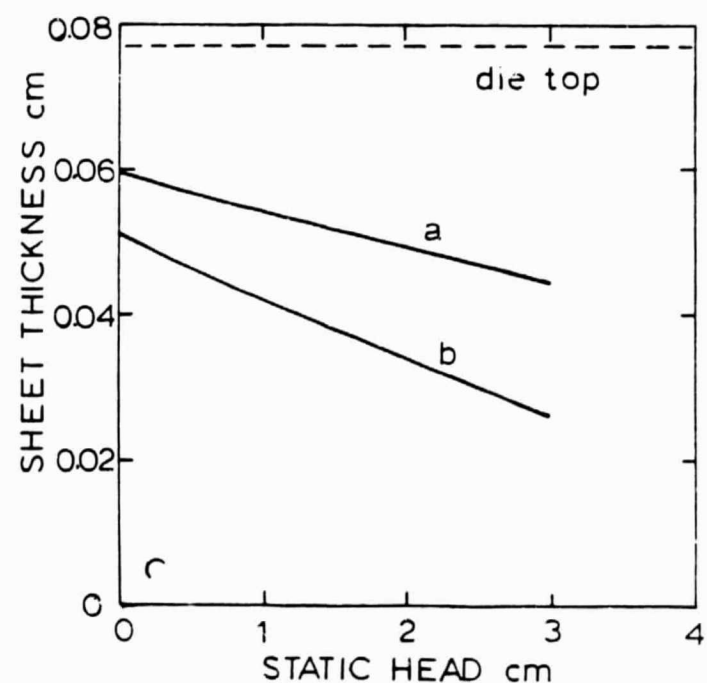
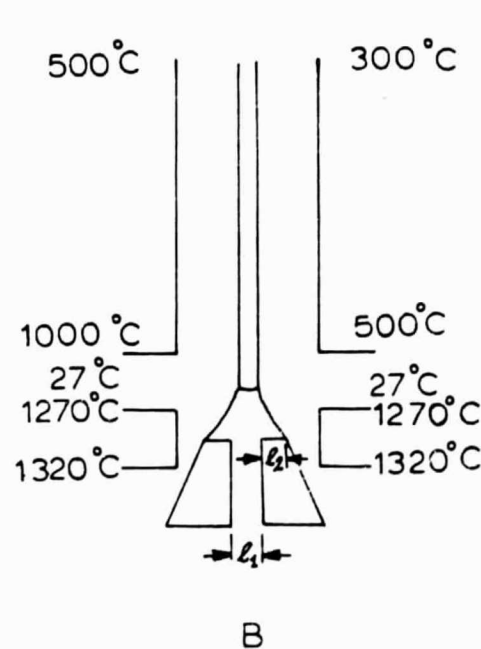
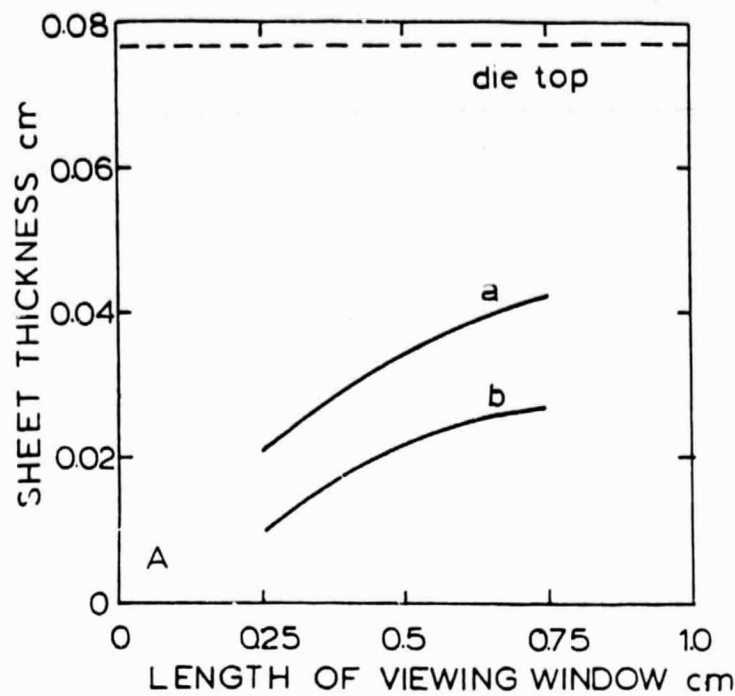


Fig. 8. (A) Effect of dimensions of the capillary spacing and die flats and length of the viewing slot on the sheet thickness for new system at capillary spacing (l_1) of: (a) 0.0254 cm and (b) 0.0662 cm. (B) Asymmetric environment temperature distribution. (C) Dependence of the sheet thickness on the static head for (a) symmetric and (b) asymmetric heat transfer surroundings.

d. Aluminum Profiles and Segregation

The successful fit of the calculated aluminum profiles and segregation along the melt/solid interface to the experimental measurements in [3] motivate the calculations presented in this section. The calculations are made along curve c of Fig. 7, using a mass diffusivity of $0.0005 \text{ cm}^2/\text{s}$ and equilibrium distribution coefficient of 0.002. The calculated melt/solid interface shapes are shown in Fig. 9(a). As is shown, the interface deflections are small and are in the same magnitude as those calculated for the cartridge system. As a result, the solute segregation caused by the growth convection is also within the same range for the results reported in [3]. The segregation profiles are given in Fig. 9(b) and as is shown, segregation varies between 10% and 20% as the growth rate is increased from 1 to 3 cm/min .

In summary, finite element models are used to analyze the new EFG system which is characterized by its simpler heat transfer configuration, that requires variations in a smaller number of parameters in order to control the growth process. The analysis is focused on relating operating conditions and states of stress. As discussed in Section 3(a), this procedure is only possible by direct connection of the heat transfer and the stress analysis calculations. This is because devising a set of arbitrary heat transfer conditions, i.e., temperature distribution, growth rate, and sheet thickness, to calculate the stress is often misleading, since the set of devised conditions may represent the growth process beyond operation limits, e.g., melt freeze at the die top, thermal supercooling. Also,

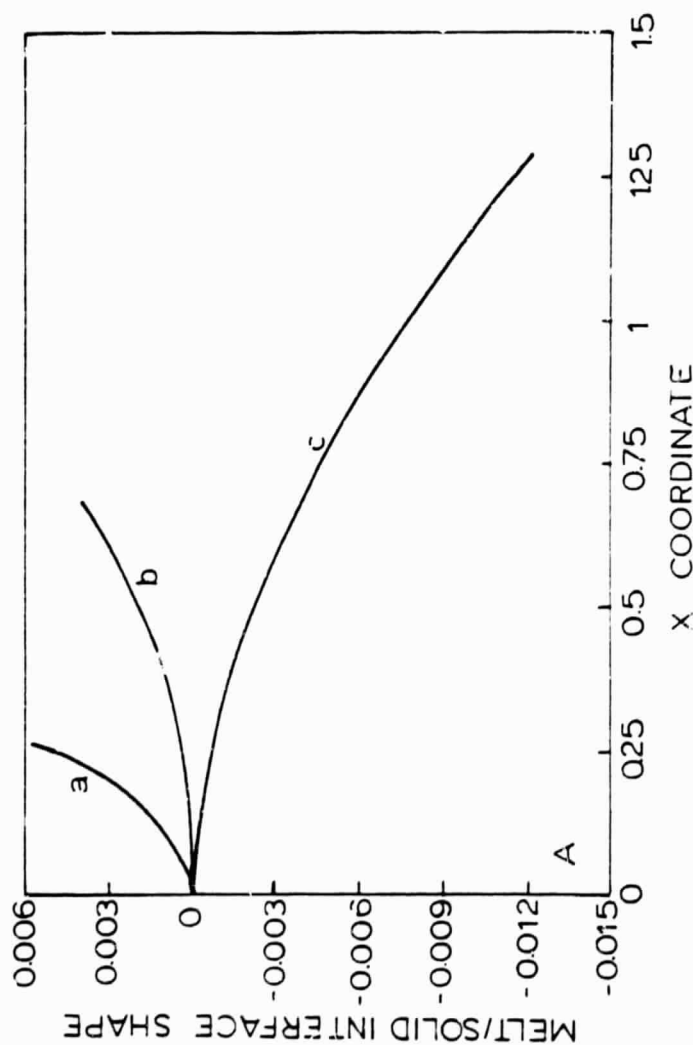
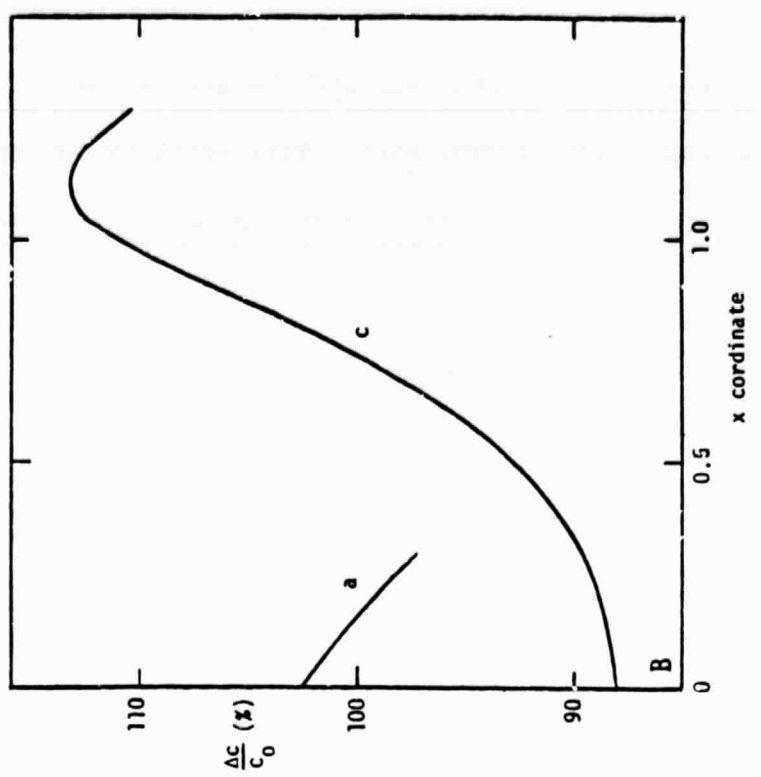


Fig. 9. Variations in (A) shapes of the melt/solid interface, and (B) aluminum profiles at growth rates of (a) 3, (b) 2, and (c) 1 cm/min.

comparison of the stresses in the cartridge and the new systems provided further insights. The thermal sensitivity analysis and mass transfer calculations complete the prediction of the system behavior.

Larger residual stresses are predicted for the new system than those calculated for the cartridge system, mainly due to the elimination of the afterheater region. In the light of this result, one may raise the following points. Given the form of the creep law used in the calculations is representative of the process of plastic deformation, the heat transfer surroundings for the new system give a higher stress configuration because the extent of creep is reduced. On the other hand, if the creep law employed does not have the appropriate form, variations in creep strength predict different stress buildup and this relationship may be different. The resolution of these issues will be provided by conducting coupled sheet growth and stress measurement experiments, where pull speed and afterheater configuration are variables.

B. EFG Defect Electrical Characterization (C. Dubé, D.B. Sandstrom, and J.I. Hanoka)

1. Introduction

The electrical activity of defects in Si is easily studied in the scanning electron microscope (SEM) with the use of electron beam induced current (EBIC). Minority carriers generated by the incident electron beam are collected by either a p-n junction or a Schottky barrier junction. The electron beam current is kept at the low 10^{-11} amps range to insure low carrier injection conditions. The induced specimen current, of the order of 10^{-7} amps for a 20 keV beam (see Fig.

10) is amplified by a fast current amplifier and the amplifier output is used to drive a CRT synchronized with the scan coils of the SEM. The resulting CRT image represents the collection efficiency for minority carriers under electron illumination. Defects present, such as dislocations or grain boundaries, act as minority carrier recombination centers, producing less collected current and hence a darker CRT image. EBIC resolution is determined by the size of the generation volume in the specimen, which depends on the incident energy of the electron beam. The resolution is about $\approx 3 \mu\text{m}$ for a 20 keV beam, $\approx 9 \mu\text{m}$ for a 30 keV beam, and $\approx 15 \mu\text{m}$ for a 40 keV beam.

Recombination enhancement, and therefore EBIC contrast enhancement, for certain defects in Si is achieved by using low temperatures ($77^0\text{K} < T < 300^0\text{K}$). In addition to providing better EBIC contrast of the defect structure, this technique can also be used to determine shallow trap energy levels associated with such defects. Further quantification of EBIC signals can be done by measuring bulk diffusion lengths, L , at various places and surface recombination velocity, S , of grain boundaries.

The aim in developing these various EBIC quantification techniques is a better understanding of the recombination properties of thermal stress-induced dislocations in silicon.

2. Sample Preparation

In order to be able to achieve the above-mentioned aim, it was first necessary to develop a thoroughly reliable method for forming Schottky barriers and ohmic back contacts for the EBIC samples. The Schottky barrier had to be sufficiently durable and reproducible for

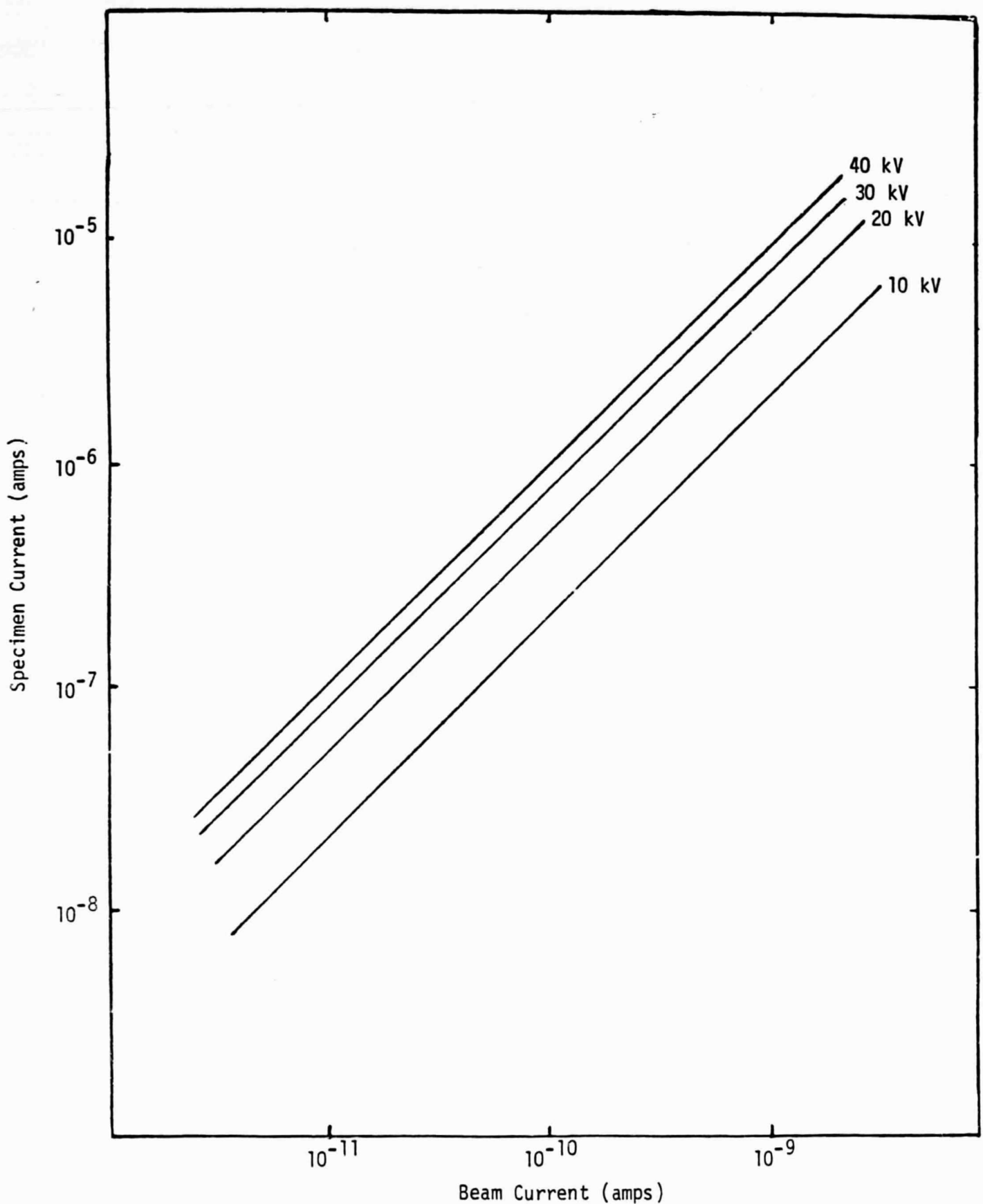


Fig. 10. Beam induced specimen current vs. beam current for a CZ solar cell.

exposure to a high energy electron beam in the SEM, but also thin enough to allow some light transmission so that a conventional surface photovoltage measurement of the diffusion length could be made to correlate to the EBIC results.

The back contact had to be made in a way which did not require any significant thermal processing of the sample as this could change the electronic properties of the material. The usual methods for forming a back contact involved evaporating Al and sintering at $T \geq 500^{\circ}\text{C}$; this was clearly too high a temperature for our requirements. Both of these areas were quite successfully addressed during this quarter of the contract.

The samples studied during this period were FZ and CZ silicon wafers stressed by four-point bending in the temperature range $1200-1400^{\circ}\text{C}$ in a previous task on this program that examined creep response.

3. Preparation of Schottky Barriers and Back Contacts

Schottky barrier preparation for EBIC analysis is preceded by an involved surface preparation step. This process is necessary to both remove any surface film deposited during the four-point bending as well as insure reproducibility in electrical characterization.

As-received FZ and CZ silicon which was stressed in Furnace 17 is characterized by a thick silicon carbide film. This film is resistant to chemical etching; however, it is readily removed by sequential polishing with 3 μm and 1 μm diamond compound. The polished surface is etched for one minute with 4-0-1 silicon etch to remove any residual polishing damage. Samples are then cleaned as follows:

- a) Boiling in $H_2O:NH_4OH:H_2O_2$ (5:1:1) for ten minutes.
- b) Rinse in deionized water.
- c) Boiling in $H_2O:HCl:H_2O_2$ (5:1:1) for ten minutes.
- d) Rinse in deionized water and blow dry.

Samples are immediately loaded into the evaporator and 200 Å of Al evaporated through a metal mask for the Schottky barrier. In future work, the use of Ti will be examined as an even more stable and durable alternative to Al for a Schottky barrier.

A back contacting scheme which did not require heating the samples above $\sim 150^{\circ}C$ was developed and found to give reproducible ohmic contacts. Details will be disclosed following a review of the patent implications of this scheme.

4. EBIC Analysis

The samples are mounted on a Cambridge Hot/Cold Stage with a top pressure contact. All EBIC work was done in a Cambridge 250 MK II SEM at either 40 keV or 20 keV. Beam current is adjusted in the 10^{-11} amp range to give a nominal specimen current of 2.0×10^{-7} amp. The signal from the diode is amplified via a Keithley 427 current amplifier and fed into the video circuit of the SEM.

After room temperature examination, the specimen is cooled to near liquid nitrogen temperature.

5. Diffusion Length Measurement

At present, there are two EBIC methods which are used in our laboratory to measure diffusion lengths, L. One method, described in a paper by Bell and Hanoka [5], assumes that a defect fills the

electron-hole pair generation sphere and varies in a smooth fashion spatially. The other method developed by Donolato [6,7] requires a grain boundary with a well-defined line scan traversing it. With the latter, diffusion lengths on either side of the grain boundary can be measured. This method is more accurate than the first method but only useful when a "well-behaved" grain boundary is present. Ultimately, we plan to determine L using both methods when we examine polycrystalline material. For the present, we will use and further quantify the first method.

In addition to the EBIC methods, in our laboratory we routinely measure L using the surface photovoltage technique (SPV). The SPV technique is rather poor for spatial resolution. The EBIC techniques, on the other hand, can have a resolution on the order of 1-15 μm , depending on the electron beam energy. Again, we plan to compare measurements made using the SPV method with those done using EBIC, particularly for dislocation-free single crystal samples where L should be spatially uniform.

6. Results

EBIC analysis of thermal stress-induced dislocations was started initially on single crystal silicon, both CZ and FZ wafers. Once the basic methods for quantification are established, then silicon sheet materials will be studied.

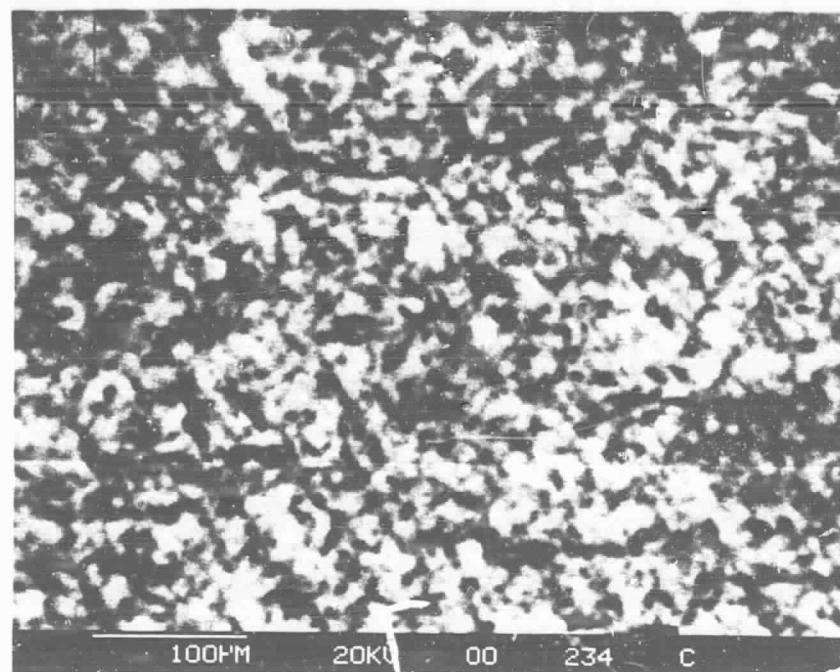
Diffusion lengths using the SPV method were measured both in the center of the stressed samples and near the edge. In general, the edge values of L were somewhat higher but all the values were quite low as can be seen in the data in Table II. Following this, room temperature

and low temperature EBIC was done on the same regions where the diffusion lengths in Table II were measured. Figure 11 shows low temperature EBIC micrographs of both the center region (top photo) and the edge region (bottom photo) for sample #S-4-26 (carbon-doped CZ). From Table II and Fig. 11, L is 4.9 μm for the center, and 4.0 μm for the edge and the dislocation densities are $\sim 7 \times 10^5/\text{cm}^2$ and $\sim 3 \times 10^5/\text{cm}^2$, respectively.

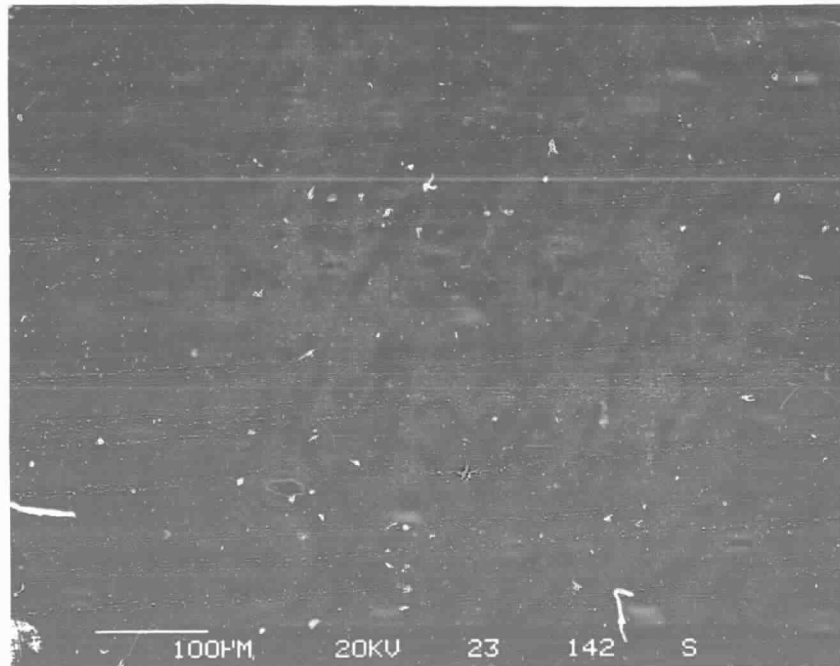
Table II. Four-Point Bending Diffusion Length Data.

Experiment Number	Material	L (μm)	
		Center	Edge
S-4-2	FZ	6.4	16.0
S-4-4	Carbon-doped CZ	2.0	12.7
S-4-4, as-received, unstressed		102.0	
S-4-21	FZ	18.3	-
S-4-22	FZ	12.8	20.5
S-4-22, as-received, unstressed		180.0	
S-4-23	FZ	11.8	14.6
S-4-23, as-received unstressed		142.0	
S-4-24	Carbon-doped CZ	6.7	10.0
S-4-26	Carbon-doped CZ	4.9	4.0
S-4-26, as-received unstressed		118.0	

It is interesting to note that both the center and edge regions of this sample showed very little EBIC contrast due to dislocations at room temperature. An illustration of this is shown in Fig. 12 where the central region is seen both at room temperature ($\sim 300^\circ\text{K}$) and at 140°K .



(a)



(b)

Fig. 11. Low temperature EBIC micrographs of (a) center and (b) edge of stressed carbon-doped CZ wafer.

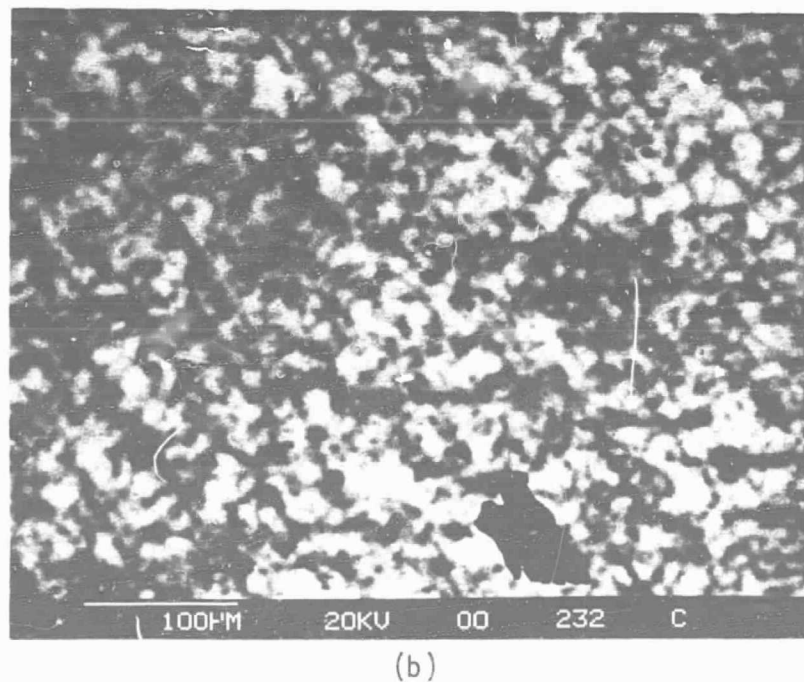
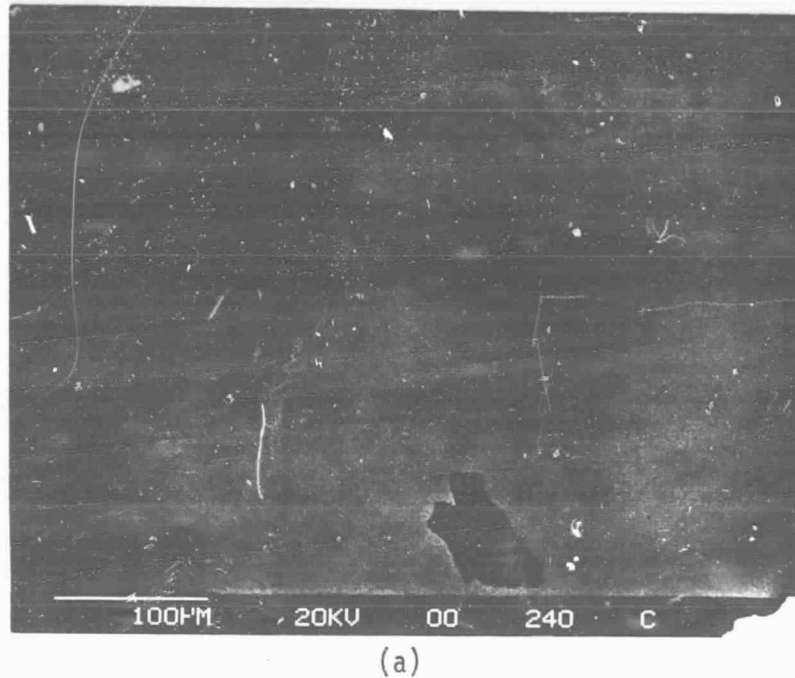


Fig. 12. (a) Room temperature, and (b) low temperature EBIC of same region for stressed carbon-rich CZ.

The question immediately arises: are the low diffusion lengths found in this stressed sample due to the high dislocation densities? And, if this is so, why is there only low temperature EBIC contrast? One piece of information which will help to answer this is the value of the diffusion length in the regions between the dislocations. That is, in the "clean", non-dislocated regions in the material. Such an approach first of all assumes that we can "abstract" the non-dislocated regions from the dislocation ones and ask what the diffusion lengths of each region might be, independent of the other region.

For instance, in Fig. 13 is shown a high magnification, low temperature (185°K) EBIC photo of the edge region shown in Fig. 11 (bottom photo). The average spacing between the electrically active dislocations is, from this photograph, $\sim 50 \mu\text{m}$. This is considerably higher than the SPV value of $4.0 \mu\text{m}$ given in Table II.

A measure of L in the non-dislocated regions, using a well-calibrated EBIC method, might then answer the question of whether point defects in the non-dislocated region are contributing to the low value of L . This will be done in future work using the method described above. In Fig. 14 is shown an EBIC line scan of the region indicated by the horizontal white line in the upper part of Fig. 13. The dips are recombination at dislocations and the flat area (arrow) is a region between dislocations where we will try to measure L .

Finally, it is interesting to note from Fig. 13 that most of the dislocations seem to be occurring in pairs. This could mean that these dislocations are parts of loops.

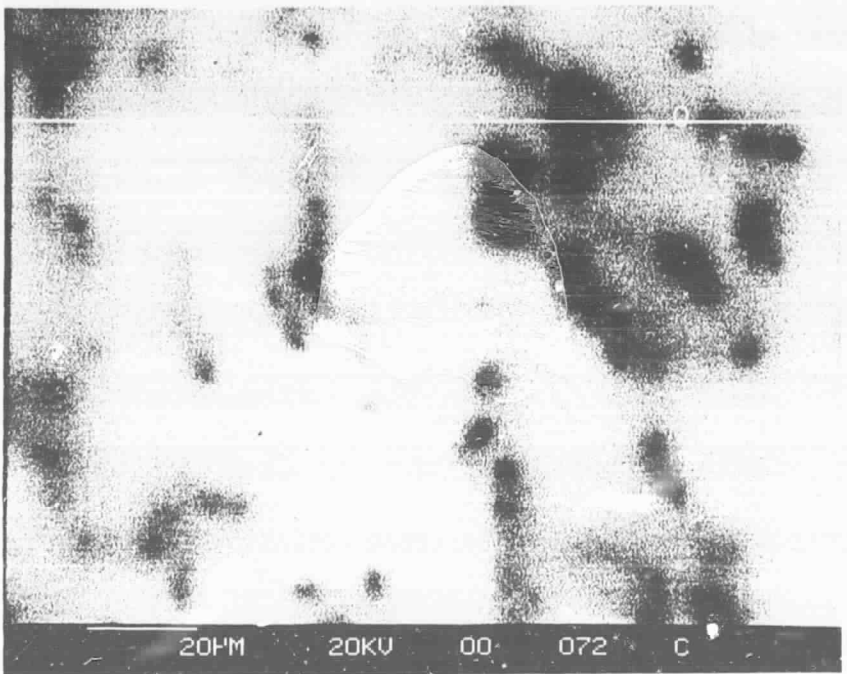


Fig. 13. High magnification EBIC micrograph of dislocations at -115°C in stressed carbon-doped CZ. Position of line scan for contrast profile is shown at top.

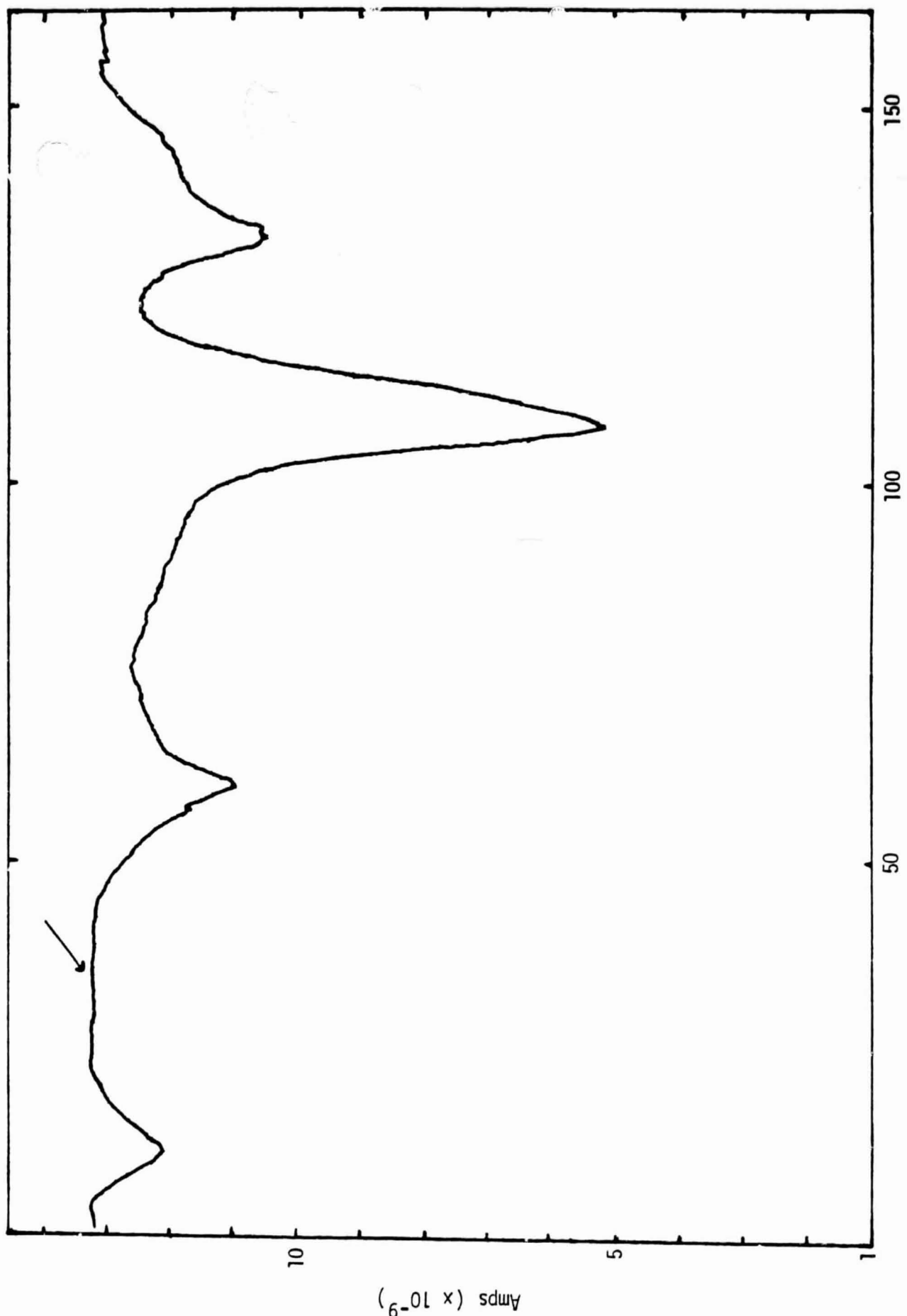


Fig. 14. Contrast profile of line scan shown in Fig. 13.

C. Creep Law Studies

An abstract was submitted to the American Conference on Crystal Growth (ACCG-6) in Atlantic City, N.J., in July. The paper was accepted for a poster presentation. The abstract is reproduced in Appendix II. Additional evaluation of the creep data generated and characterization of defects are underway.

D. Residual Stress Measurements

The most recent results on stress measurements carried out at the University of Illinois are reported in Appendix III.

References

1. J.C. Lambropoulos, J.W. Hutchinson, R.O. Bell, B. Chalmers, and J.P. Kalejs, "Plastic Deformation Effects by Stress Generated During Silicon Sheet Growth at High Speeds", *J. Crystal Growth*, 65 (1983).
2. H.M. Ettouney, R.A. Brown, and J.P. Kalejs, "Analysis of Operating Limits in Edge-Defined Film-Fed Growth", *J. Crystal Growth*, 62 (1983), 230-246.
3. H.M. Ettouney, J.P. Kalejs, and R.A. Brown, "Comparison of Finite Element Calculations and Experimental Measurements in Edge-Defined Film-Fed Growth of Silicon Sheets", *J. Crystal Growth*, submitted, 1984, and given in Appendix I.
4. J.P. Kalejs, B.H. Mackintosh, and T. Surek, "High Speed EFG of Wide Silicon Ribbon", *J. Crystal Growth*, 50 (1980), 175-192.
5. R.O. Bell and J.I. Hanoka, *J. Appl. Phys.*, 53(3), 1741 (1982).
6. C. Donolato, *Appl. Phys. Lett.*, 34, 80 (1979), and C. Donolato, *Scan. Electron Microscopy*, Part I (1979), p. 257.
7. C. Donolato and R.O. Bell, *Rev. Sci. Instrum.*, 54(8), 1005 (1983).

APPENDIX I

Paper entitled "Comparison of Finite Element Calculations and Experimental Measurements in Edge-Defined Film-Fed Growth of Silicon Sheets" by H.M. Ettonney, J.P. Kalejs and R.A. Brown.

To be presented at ACCG-6/ICVGE-6, Atlantic City, N.J., July 16-20, 1984, and paper to be published in the volume of Conference Proceedings in the Journal of Crystal Growth.

COMPARISON OF FINITE ELEMENT CALCULATIONS AND EXPERIMENTAL
MEASUREMENTS IN EDGE-DEFINED FILM-FED GROWTH OF SILICON SHEETS

H.M. Ettouney, J.P. Kalejs

Mobil Solar Energy Corporation
16 Hickory Drive
Waltham, Massachusetts 02254, U.S.A.

and

R.A. Brown

Department of Chemical Engineering
Massachusetts Institute of Technology
Cambridge, Massachusetts 02139, U.S.A.

ABSTRACT

Predictions of finite element analysis of heat and solute transfer in Edge-defined Film-fed Growth (EFG) of silicon sheets are compared to experimental measurements of crystal thickness, growth rate limits and solute segregation in 10 cm wide ribbon growth. The calculations are based on the two-dimensional thermal-capillary model of Ettouney et al. (J. Crystal Growth 62 (1983), 230) combined with an empirical model for the growth system temperature distribution and full solution of the convective transport equations for determining dopant segregation. The prediction of ribbon thickness as a function of growth rate is excellent for the entire speed range accessible with the system. The thermal-capillary limit for growth rate of 4.3 cm/min obtained from the model also agrees with the observed maximum rate where the ribbon detached from the melt. Aluminum segregation across the ribbon thickness, as measured by spreading resistance, is accurately predicted as a function of growth rate when the possibility of surface-tension-driven convection is ignored.

1. Introduction

The development of growth processes for silicon sheet used in photovoltaic cells has reached the point where the engineering optimization of each technique with respect to crystal quality and areal growth rate will determine its economic feasibility [1-3]. Mathematical modeling can play an important role in this optimization by differentiating the operating characteristics of different growth processes and by predicting optimal process variables. The limits on growth rate, dictated by process stability, the relationship between sheet thickness and process variables, and the degree of compositional uniformity attainable in meniscus-defined growth systems, depend on the interactions between the temperature field in the melt, crystal and die and the shapes of the melt/gas and melt/solid interfaces. Each interaction is described by the solution of detailed mathematical models for heat and mass transport and meniscus shape. Moreover, the degree of crystalline perfection in the grown material is coupled by the thermally-induced stress field to the thermal environment and by the influence of dopants on defect generation to the transport of impurities in the melt.

The purpose of this paper is to report the detailed comparison of calculations and experiments for the Edge-defined Film-fed Growth (EFG) technique for silicon sheet and by doing so to establish the level of detail needed for quantitative prediction of measured properties of such a system.

We have presented finite element calculations dealing with the central aspects of heat transfer, capillarity and solute segregation

for the EFG technique in a recent series of publications [4-7]. The thermal-capillary analysis presented in [4] combines a two-dimensional model for conduction-dominated heat transfer in each phase and radiation and convection to the surroundings with determination of the meniscus shape by capillary statics, as given by the Young-Laplace equation with conditions for equilibrium attachment at the melt/crystal/gas and melt/die/gas tri-junctions. The heat transfer model is based on the assumptions that heat transfer along the width of the ribbon is uniform, that the ribbon is much wider than its thickness, and that details of convective heat transfer are unimportant for predicting crystal dimensions and melt/solid interface shape. The validity of the assumed uniformity of heat transport along the width of the die depends on the precision of the experimental equipment; this point is addressed more in Section 3.1. Typical ribbons are over one hundred times wider than the thickness. The assumption for simplifying convective heat transfer has been validated for silicon growth [6] by comparison of the results of the conduction-dominated model with calculations that included fluid mechanics of the melt when thermocapillary motion was not present. The importance of these approximations is discussed further below.

The calculations predict the crystal thickness, meniscus height, and temperature field as a function of die geometry, growth rate and thermal operating conditions. For a specified thermal environment, the wetting conditions at the top of the die surface, combined with the constraints of heat transfer and capillarity, set operating bounds for steady-state operation that dictate the maximum growth rate for a given

static head h_{eff} . Rate limits have been observed in practice and many of the possible causes have been addressed by Chalmers [8]. We have analyzed the bounds on operation of an idealized EFG system in the papers [4,9]. Of particular interest here is the prediction from Ref. [9] of a limit in static head for the existence of steady-state ribbon growth for fixed growth rate. This limit is caused by the coupled actions of heat transfer through the melt and ribbon, and of the surface tension which shapes the meniscus.

Modeling of dopant segregation across the thickness of the ribbon involves accurate prediction of the shape of the meniscus, of the configuration of the melt/solid interface, and of the fluid flow field within the melt. We follow the approach developed in Ref. [7] and use the melt shape predicted from the heat transfer analysis as the domain for full finite element calculation of the velocity field and dopant distribution in the melt. Because of the low mass diffusivities D characteristic of dopants in silicon (D for aluminum is 5×10^{-4} cm²/sec), Peclet numbers for solute transfer, $Pe_m = V_g L^*/D$, based on a characteristic length scale $L^* = 0.025$ cm, at typical EFG growth rates V_g are near unity. The details of the velocity field are thus important in setting segregation. Besides the flows induced solely by crystal growth, surface-tension-driven motions caused by the large temperature gradient along the meniscus may also add to convection in the melt. Calculations in Ref. [7] for temperature gradients characteristic of EFG and for surface tension variations with temperature of a uncontaminated silicon/gas interface suggest that thermocapillary velocities are 100 times faster than typical growth

speeds. We compare segregation calculations with and without thermocapillary flows to measurements of aluminum segregation in Section 3.3.

The comparison between the finite element calculations and experimental data for silicon sheet growth by EFG is based on the cartridge system for 10 cm wide ribbon which has been under development for its potential to significantly increase the areal sheet production rate [2,3]. The details of the experimental system and the thermal boundary conditions used to model it are presented briefly in Section 2 and the results of the comparison are given in Section 3.

2. Finite Element Model and Experimental System

Linking numerical calculations directly to experimental systems requires accounting for complexities in the heat transfer caused by the real radiation fields adjacent to the die, melt and sheet. For example, in the 10 cm EFG cartridge system to be examined here, efforts to minimize stress arising from enhanced growth rates promoted by a cooler have been successful through introduction of a reheat or afterheater region, as illustrated in Fig. 1. In addition, in most growth geometries, the region between the die base of approximately constant temperature \tilde{T}_0 and the cooler, as in Fig. 1, is difficult to model because of complicated arrangements of die top shields and view slots. The heat transfer effects arising from these aspects of system design are represented here by an environmental temperature distribution $\tilde{T}_\infty = \tilde{T}_\infty(y)$, with $\tilde{T}_\infty(0) \equiv \tilde{T}_0^0$, where y is the axial coordinate, and interpolation schemes are used that are consistent with known temperatures of system components when environment temperatures

are not known. The sheet thermal conductivity is taken to be temperature dependent according to the relation $k_s(\bar{T}) = k_m T_m/\bar{T}$, where $k_m = 0.22 \text{ W/cm-K}$ is the conductivity at the melting point. The other thermophysical properties have values the same as those given in Table 2 of Ref. [4]. Full solutions of the Navier Stokes equations for the melt flow field in the die capillary and meniscus are used in calculating interface dopant segregation according to the scheme reported previously [7].

The other details of the mathematical model and the finite element solution procedure follow directly the approach laid out in Ref. [4]. The finite element mesh used was the same as mesh I presented in Ref. [4] and had 600 elements and 671 unknown coefficients for temperature. The accuracy of this discretization is discussed there. The calculations were performed on the Data General MV4000 computer in the Department of Chemical Engineering at MIT using double precision arithmetic.

2.1. 10 cm Cartridge System

Experimental data for the variation of ribbon thickness with growth speed and for impurity segregation through the thickness were obtained for 10 cm wide ribbon grown from a cartridge of the general design described in Ref. [10], and shown schematically in Fig. 1. The static head h_{eff} was 4 cm for the experiments. The melt was doped with aluminum which has a sufficiently low segregation coefficient ($k = 0.002$) such that its redistribution is very sensitive to the interface configuration and to the flow field. Electrical activity changes produced by segregation response to growth condition variations were

monitored by two-point probe spreading resistance measurements taken on bevelled sections through the ribbon thickness.

The temperature distributions of the cooler and the heater were measured in place by thermocouples and ambient temperatures of the regions between these elements were set by linear interpolation. Once a value for the ambient temperature at the die base \tilde{T}_∞^0 was assumed, the ambient temperature field between it and the cooler temperature was also set by linear interpolation. A typical temperature distribution for the sheet environment and a calculated axial profile are shown in Fig. 2. The model of the thermal environment for the die top is completed by the specification of the setpoint temperature at the base of the die, \tilde{T}_0 . This temperature represents a measure of the power input into the die from resistance heating and is the principal unknown for the experimental system. Thermocouple measurements of the temperature of the die suggest that \tilde{T}_0 will range between 25° and 50°C above the melting temperature of silicon.

3. Comparison of Model and Experimental Results

3.1. Sheet Thickness as a Function of Growth Rate

Silicon ribbon was grown continuously over a range of growth rates at fixed thermal conditions for the system, and thickness profiles across the width were obtained at several locations for each speed. Measurements of thickness as a function of growth rate for a thick and a thin region of a 10 cm wide ribbon are compared to model predictions in Fig. 3. The severe thickness variations reflected in the data arise occasionally because of die top silicon spills or system component misalignments which lead to temperature differences along the

die top. The setpoint temperature at the die base \tilde{T}_0 has been used as the adjustable variable to fit the model predictions, with \tilde{T}_∞^0 fixed at 1733 K. The change in \tilde{T}_0 required to account for the thickness variation across the ribbon width is 9°C. Model predictions are shown also for the case when \tilde{T}_0 is kept fixed at the value for best fit of the lower data points and \tilde{T}_∞^0 is varied to obtain a 50% increase in thickness (dashed curve). The large changes in the ambient temperature \tilde{T}_∞^0 necessary to produce such thickness variations are outside of the realistic range of variations in surface temperatures in the die environment. This sensitivity analysis illustrates that \tilde{T}_0 is the controlling variable for producing a fit of the model results to the experimental data and that fluctuations in die top temperature are primarily responsible for sheet nonuniformity. This conclusion was previously also reached in the analysis of asymmetric die EFG [11].

3.2. Growth Rate Limits

The finite element calculations predict that steady-state growth of silicon sheets is not possible outside a relatively narrow window in terms of combinations of growth rate V_g and static head h_{eff} . For set growth rate, increasing the static head thins the meniscus and the sheet until the area for conductive heat transfer severely constricts the heat conduction through the sheet. This thermal-capillary limit, described in detail in [9], results in loss of steady-state growth.

The operating diagram for crystal thickness as a function of growth rate V_g and static head h_{eff} calculated for the ribbon system modeled here is shown in Fig. 4(a) for a range of static heads and

growth rates between 2.5 and 4.5 cm/min. The thermal-capillary limit for each growth rate is at the value of h_{eff} where the curve of predicted sheet thickness becomes vertical with respect to small changes in static head. We have used computer-aided perturbation analysis [9] to show that the family of steady-state solutions reverses directions in h_{eff} at this point and that the solutions on the reverse portion of the curve are unstable. The locus of these limit points shown on Fig. 4(a) is a bound on the operating range for the EFG system. The calculations predict a limiting growth rate of 4.3 cm/min at a static head of 5.3 cm for the values of T_0 and \tilde{T}_∞^0 used to fit the lower curve in Fig. 3. This maximum growth rate is in good agreement with the approximate measured maximum of 4.3 cm/min where the meniscus separated from the die top (vertical dotted line at $h_{eff} = 4$ cm in Fig. 4(a)).

The loss of existence of the finite element solution beyond the maximum growth rate does not indicate the dynamics for failure of the growth system. The separation of the meniscus from the die top can be equally well explained by a decrease in the angle made by the melt at the die top below the equilibrium contact angle for the melt/die/gas contact. We have investigated this possibility by computing this angle for the values of static head and pull speed shown in Fig. 4(a); the computed angles are plotted in Fig. 4(b). A significant prediction of the model is that the thermal-capillary limit becomes more restrictive than the Gibbs limit for contact angle below a static head of about 6.5 cm for this system as it is operated at increasingly higher speeds.

3.3. Aluminum Segregation

Finite element calculations of the melt velocity field and aluminum segregation were performed to model the steady-state growth experiments using melt/solid and melt/gas interface shapes predicted from the thermal-capillary analysis discussed above. Calculations were carried out assuming initially that solidification flow was the sole mechanism driving melt flow and were compared to results including thermocapillary flows driven by the axial temperature gradient along the meniscus. When the growth rate approaches the maximum melt velocity, the Peclet number Pe_m may be as high as ten, and the finite element calculations of aluminum segregation are straightforward even for the low value of its partition coefficient. Thermocapillary flows increased the characteristic velocity by a factor 100 and calculations of dopant segregation for the actual temperature gradients were then impossible.

Melt/solid interface shapes ($h(0) - h(x)$), scaled by $L^* = 0.025$ cm, predicted by the model are shown in Fig. 5 for the conditions of growth represented by the fit with $\tilde{T}_o = 1721$ K in Fig. 3. For impurities with segregation coefficients less than unity, these interface configurations result in higher concentrations at the ribbon centerline than at the surface, as discussed in [12,13]. The converging melt flow caused by the tapering of the meniscus enhances the radial segregation above that associated with the interface curvature for typical EFG process conditions [11]. This makes the segregation also dependent on the meniscus configuration, and requires the complete thermal-capillary solutions to correctly model the

influences of the growth speed and thickness on impurity redistribution. The interface shapes shown in Fig. 5 qualitatively reproduce shapes characteristic of the EFG cartridge system, as observed using ribbon grown from antimony-doped melts that allow interface demarcation [14].

The streamlines and concentration fields in the meniscus and die top melt for aluminum, corresponding to two of the interface configurations of Fig. 5, are given in Figs. 6(a) and 6(b), respectively. The isoconcentration lines are parameterized by $c(x,y) = \bar{c}(x,y)/c_0$, where c_0 is the bulk melt concentration. These cases show the extent to which the tapering of the meniscus and the resulting convergent flow make the solute distribution in the meniscus depart from a one-dimensional profile. The magnitude of the radial interface segregation, as measured by the concentration difference $\Delta c = 100 k |c(0, h(0)) - c(t, h(t))|$ decreases with increasing growth rate; for the range between 2.5 cm/min and 4.0 cm/min modeled, Δc varies between 12.3 and 6.9 for aluminum.

Spreading resistance profiles through the thickness taken on the same aluminum-doped ribbon used to generate the lower set of data in Fig. 3 for 2.5 and 3.5 cm/min are given in Fig. 7. The radial segregation predicted at these speeds and at the die temperature $\bar{T}_0 = 1721$ K (solid curves in Fig. 7) reproduce both the magnitude and dependence of the experimental data on growth rate, excluding spikes caused by structural defects, such as observed in Fig. 7(a).

Thermocapillary flows arise in the melt from shear stress at the melt/gas interface created by changes in the surface tension with

temperature. The velocity scale appropriate for thermocapillary motion is defined as $V = (d\sigma/d\tilde{T})\Delta\tilde{T}^*/\mu$ where $d\sigma/d\tilde{T}$ is the change in surface tension with temperature, μ is the viscosity of the melt, and $\Delta\tilde{T}^*$ is the temperature difference between the die top and the melt/solid interface which determines the strength of the thermocapillary driving force. Hardy [15] has measured $d\sigma/d\tilde{T}$ to be approximately 0.22 dynes/cm-K for silicon. For a typical silicon EFG system, $V = 120$ cm/sec, three orders of magnitude greater than the growth velocity.

The extremely high velocities associated with the thermocapillary motion make finite element calculations of mass transfer difficult for realistic driving forces. We have performed calculations using the scheme defined in Ref. [7] for a dopant with $k = 0.1$ and with $d\sigma/d\tilde{T} = 0.01$ dynes/cm-K, one-twentieth of the reported value for silicon. The calculated thermocapillary flow greatly distorts the concentration field throughout the melt and produces significantly enhanced radial segregation at the interface; Δc is 41.4 for a growth rate of 2.5 cm/min, compared to the value 12.3 predicted for $k = 0.002$ neglecting thermocapillary motion. At a higher growth rate of 4.0 cm/min, the dopant concentration in the bulk melt was almost uniform along the meniscus, except close to the melt/solid interface and the die top.

Although calculations with still higher values of $d\sigma/d\tilde{T}$ lead to increasing segregation Δc in disagreement with experiment this alone cannot definitely rule out the presence of surface-tension-driven flows. As demonstrated in [7], a mass transfer boundary layer will form along the melt/crystal surface when convection is increased further and eventually will lead to more uniform dopant distributions

along this interface. These calculations suggest that even more vigorous flows than created by the correct value of $d\sigma/d\tilde{T}$ will be needed to reduce lateral segregation to the level observed in the experiments. However, visual observations of the melt/gas surface during growth give no indication that such strong flows are present during growth.

4. Summary

The thermal-capillary model applied to the 10 cm EFG cartridge system predicts the dependence of ribbon thickness on growth rate, growth rate limits, and aluminum segregation across the ribbon in terms of a single unknown parameter, the temperature at the base of the die \tilde{T}_0 . Each of these variables compares favorably with experimental data for a single value of \tilde{T}_0 specific for a location across the width of the die. The values of \tilde{T}_0 used are also in accord with thermocouple measurements taken adjacent to the die bottom. When taken together, these results indicate that all the transport phenomena and capillary physics important in the EFG process are being accounted for quantitatively in the models used.

With the exception of the modeling of the radiative transfer between the ribbon and its surroundings, heat transfer is computed strictly from first principles so that the strategies used for modeling EFG are readily adapted to other meniscus-defined growth systems. The radiative interactions between the die, melt, crystal and surroundings are modeled by an axial ambient temperature profile $\tilde{T}_\infty(y)$, which is based on experimental measurements. Analytical techniques have been developed [16] to include explicitly details of radiative heat transfer

from the surroundings and in the sheet and have been applied to the calculation of stress in the 10 cm ribbon [3]. Incorporation of these improvements into the finite element heat transfer model is underway.

Acknowledgements

We gratefully acknowledge the assistance of M.C. Cretella and A.A. Menna in obtaining experimental data presented here.

This paper is based on work sponsored in part by the Jet Propulsion Laboratory, California Institute of Technology, under Subcontract No. 956312.

References

- [1] W.T. Callaghan, Proceedings of 15th IEEE Photovoltaic Specialists Conference (IEEE: New York; 1981), p. 361.
- [2] J.P. Kalejs et al., Final Report, DOE/JPL 954355/81/21 (September, 1982) (unpublished).
- [3] J.C. Lambropoulos, J.W. Hutchinson, R.O. Bell, B. Chalmers, and J.P. Kalejs, *J. Crystal Growth*, 65 (1983), 324.
- [4] H.M. Ettouney, R.A. Brown, and J.P. Kalejs, *J. Crystal Growth*, 62 (1983), 230.
- [5] J.P. Kalejs, H.M. Ettouney, and R.A. Brown, *J. Crystal Growth*, 65 (1983), 316.
- [6] H.M. Ettouney and R.A. Brown, in: Proceedings of the Flat-Plate Solar Array Project Research Forum on High Speed Growth and Characterization of Crystals for Solar Cells, ed. K.A. Dumas, DOE/JPL-1012-95 (April, 1984), p. 31i (unpublished).
- [7] H.M. Ettouney and R.A. Brown, *J. Appl. Physics*, 55 (1984), 4384.
- [8] B. Chalmers, in: Proceedings of the Flat-Plate Solar Array Project Research Forum on high Speed Growth and Characterization for Growth of Solar Cells, ed. K.A. Dumas, DOE/JPL-1012-95 (April, 1984), p. 15 (unpublished).
- [9] H.M. Ettouney and R.A. Brown, *J. Crystal Growth*, submitted 1984.
- [10] J.P. Kalejs, B.H. Mackintosh and T. Surek, *J. Crystal Growth*, 50 (1980), 175.
- [11] J.P. Kalejs, L.-v. Chin and F.M. Carlson, *J. Crystal Growth*, 61 (1983), 473.
- [12] S.R. Coriell and R.F. Sekerka, *J. Crystal Growth*, 46 (1979), 479.
- [13] S.R. Coriell, R.F. Boisvert, R.G. Rehm, and R.F. Sekerka, *J. Crystal Growth*, 54 (1981), 167.
- [14] C.V.H.N. Rao, M.C. Cretella, F.V. Wald and K.V. Ravi, *J. Crystal Growth*, 50 (1980), 311.
- [15] S.C. Hardy, U.S. Department of Commerce Publication, Materials Measurements, NBSIR 83-2772 (1983).
- [16] R.O. Bell (unpublished).

Figure Captions

Figure 1. Cross-sectional schematic of EFG cartridge system for 10 cm wide ribbon. The model dimensions shown are: $l_1 = 0.005$ cm, $l_2 = 0.15$ cm, $l_3 = 0.025$ cm, $l_4 = 0.25$ cm, $l_5 = 4.25$ cm, $l_6 = 0.45$ cm, $l_7 = 0.3$ cm, $l_8 = 0.5$ cm, and $l_9 = 3$ cm.

Figure 2. Temperature distribution of the environment surrounding die, meniscus and ribbon along the centerline, and typical calculated ribbon profile. The temperature scale is normalized to $\tilde{T}^* = 1783$ K, and the length scale to $L^* = 0.025$ cm.

Figure 3. Crystal thickness as a function of growth rate compared for experiments and calculations. Dashed curve (---) shows sensitivity of finite element results to the environment temperature near the die base, T_∞^0 . Melt interface temperature gradients predicted by the calculations are also plotted for the lower curve.

Figure 4(a). Variation of crystal thickness with growth rate V_g and static head h_{eff} predicted by finite element calculations for experimental system.

(b). Apparent contact angle Θ_c at the edge of the die for configurations in Fig. 4(a).

Figure 5. Predicted variation of the melt/solid interface shape as a function of growth rate. The length scale is normalized to $L^* = 0.025$ cm.

Figure 6(a). Streamlines for flow field driven solely by solidification flow.

(b). Isoconcentration contours for the flows shown in Fig. 6(a).

Figure 7. Spreading resistance profiles for aluminum-doped ribbon grown at (a) 2.5 cm/min and (b) 3.5 cm/min. Traces are for the locations across the ribbon represented by the lower set of data in Fig. 3 and were taken down a $2^{\circ} 52'$ bevel through the ribbon thickness. The length scale is normalized to $L^* = 0.025$ cm.

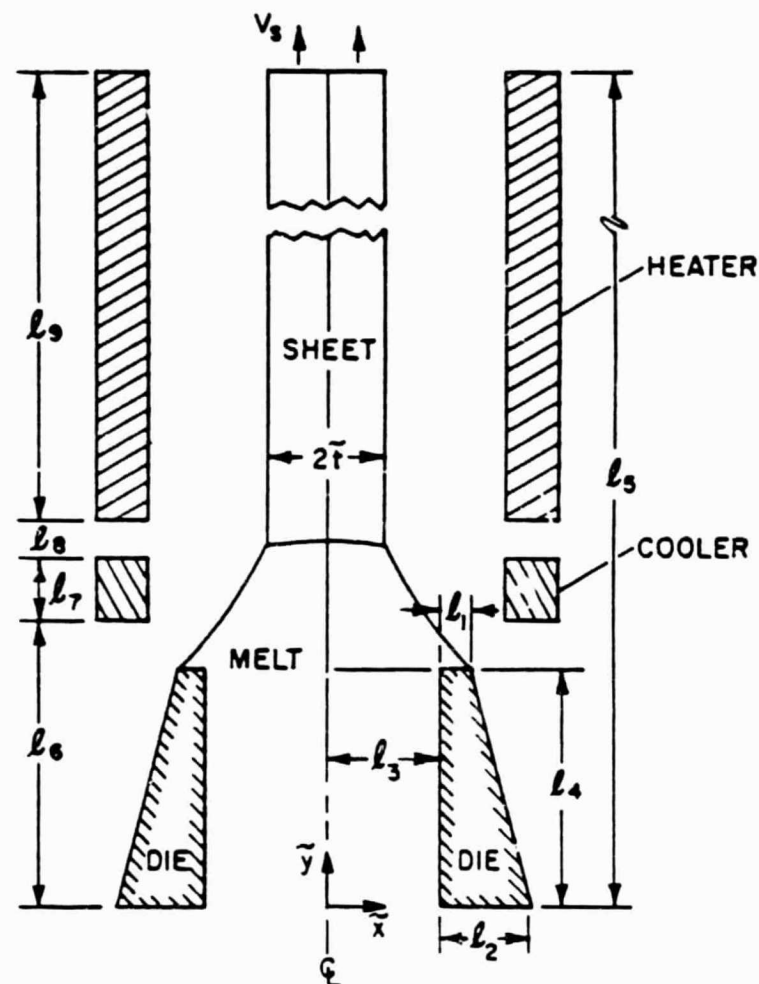


Figure 1

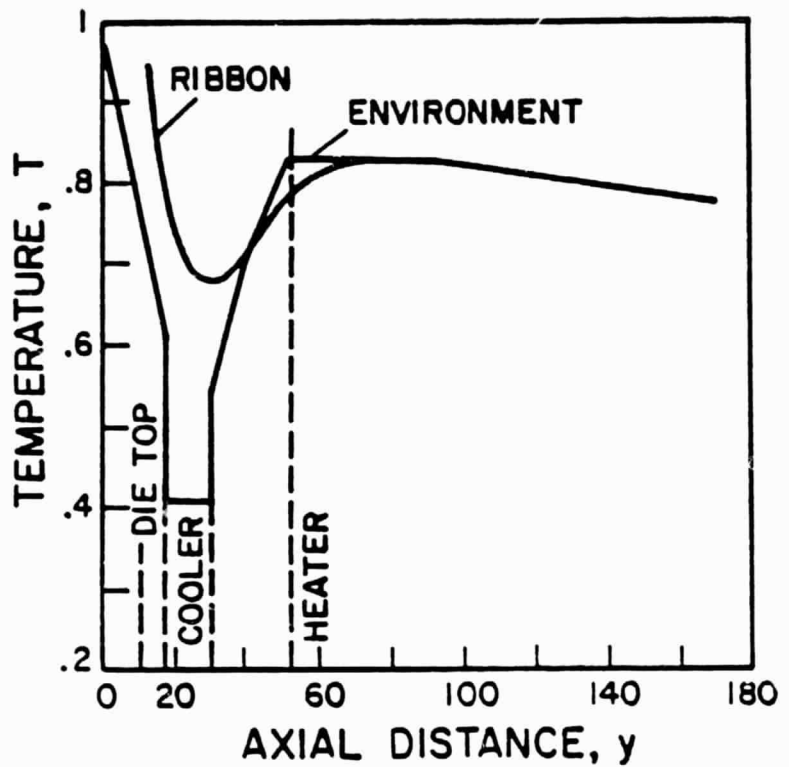


Figure 2

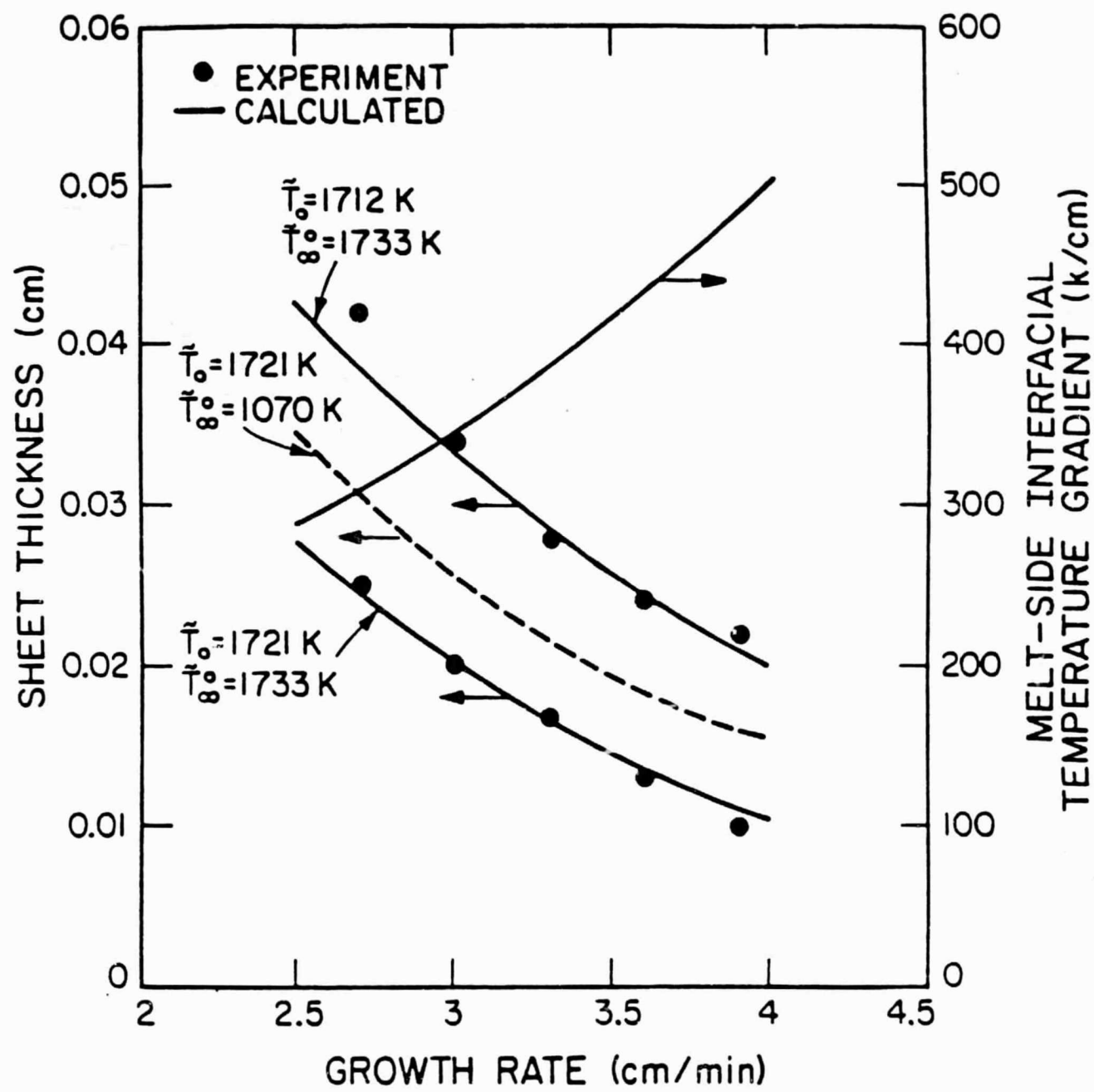


Figure 3

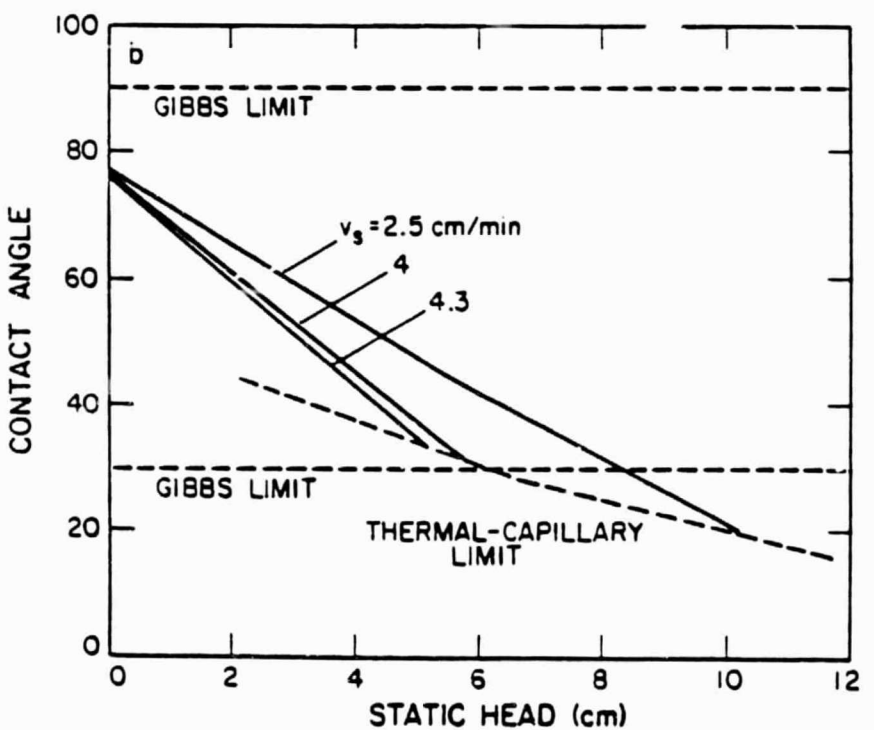
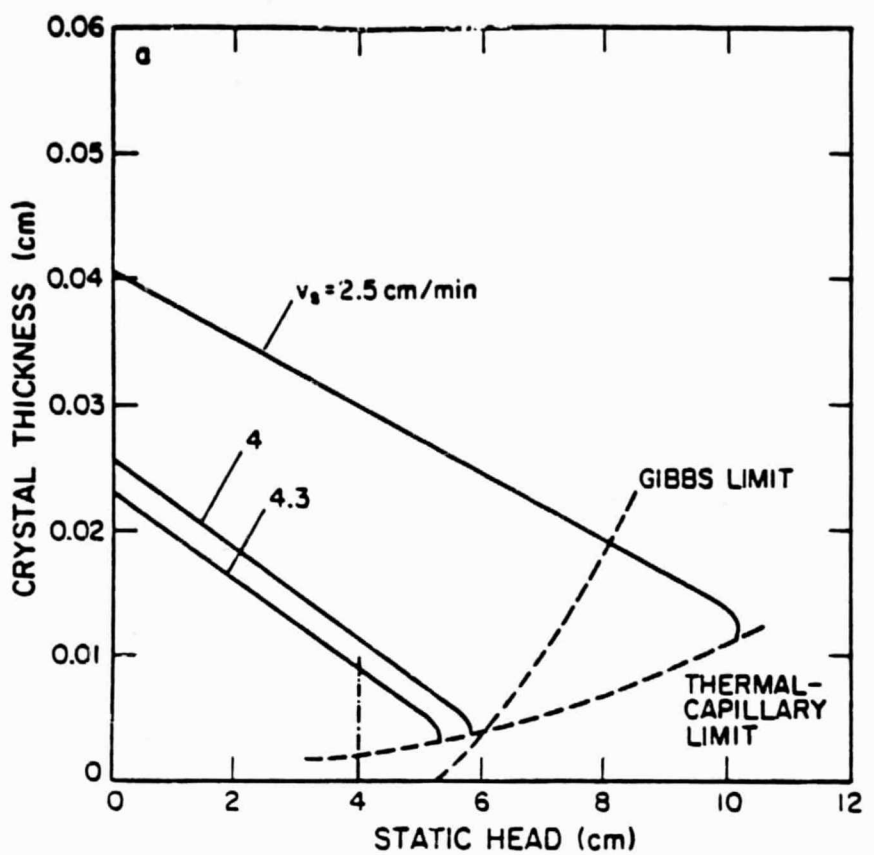


Figure 4

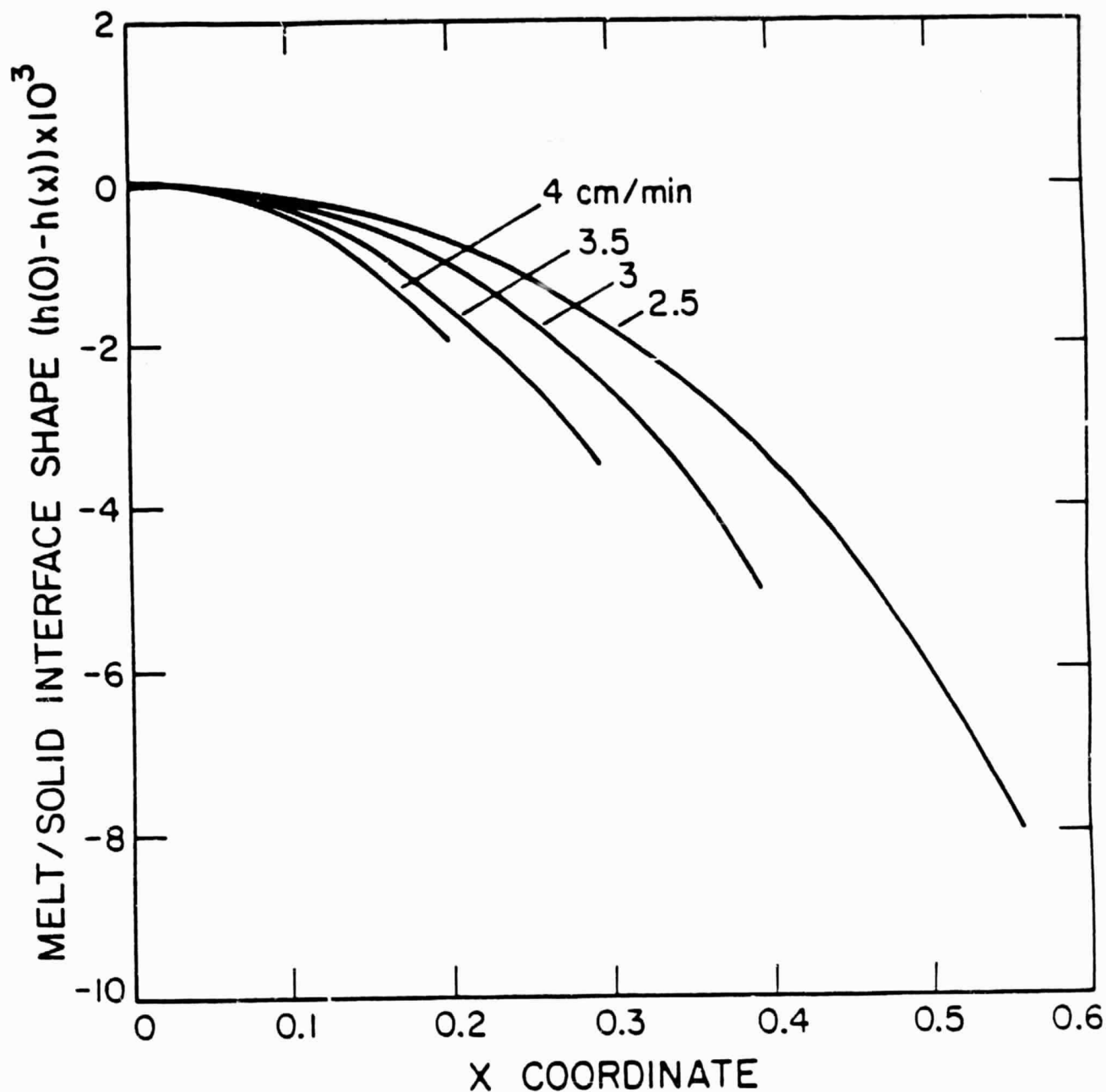


Figure 5

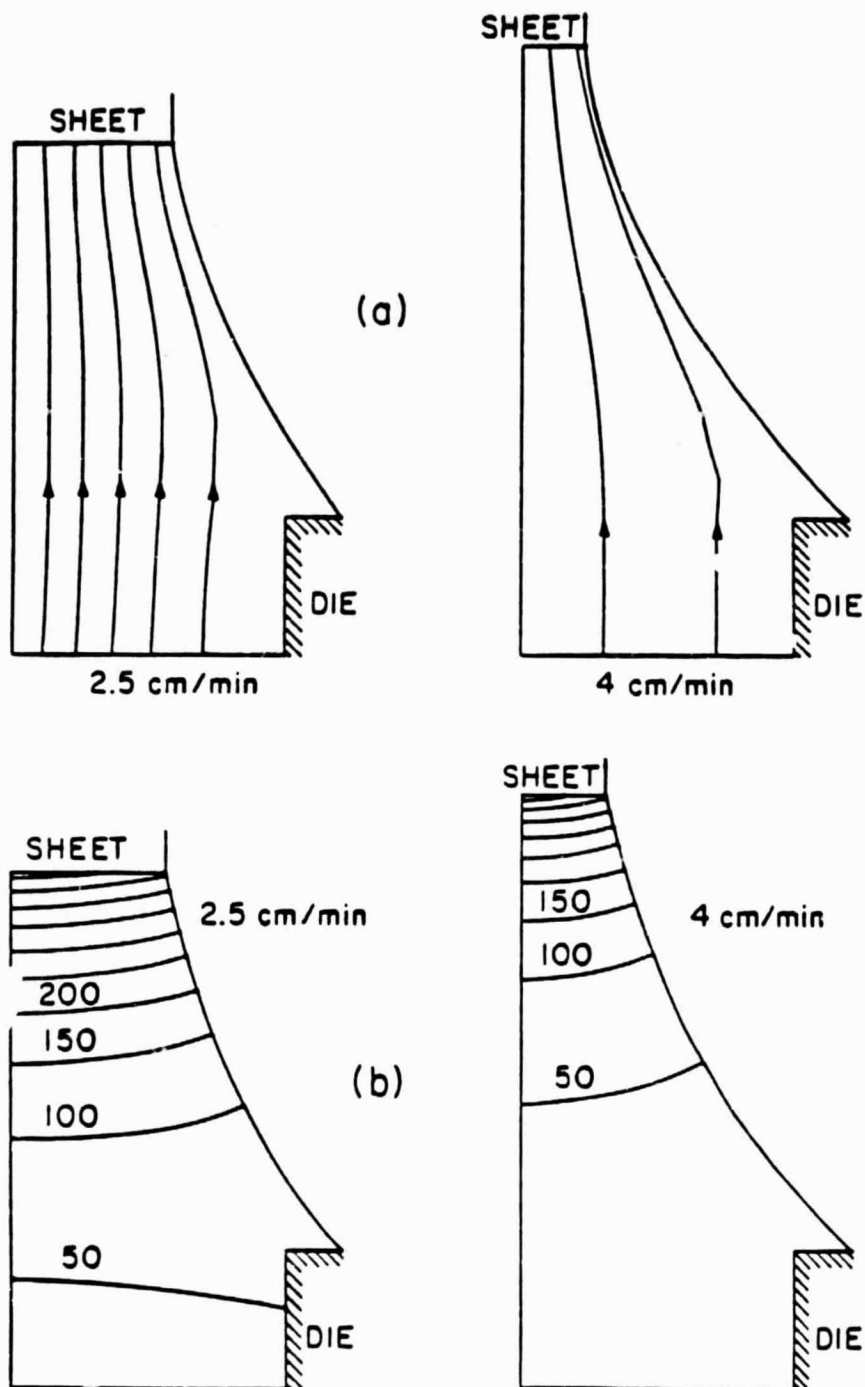


Figure 6

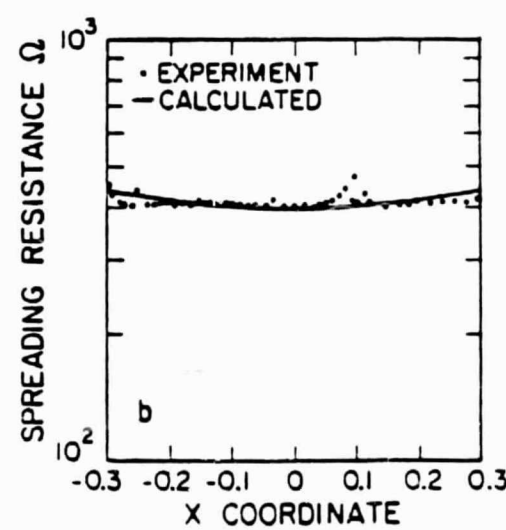
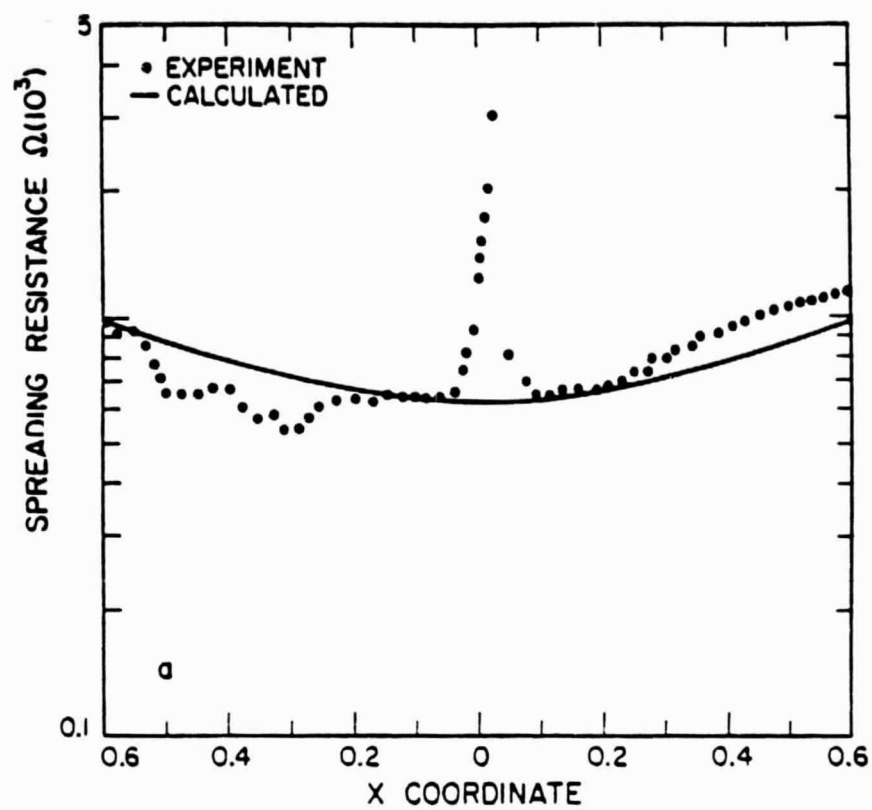


Figure 7

APPENDIX II

Abstract of poster presentation "Primary Creep Studies in Silicon Above 1200°C and Application to High Speed Sheet Growth", by J.P. Kalejs, A.A. Menna, M.C. Cretella and N.W. Marr.

To be presented at ACCG-6/ICVGE-6, Atlantic City, N.J., July 16-20, 1984.

APPENDIX II

PRIMARY CREEP STUDIES IN SILICON ABOVE 1200°C AND APPLICATION TO HIGH SPEED SHEET GROWTH†

J.P. Kalejs*, A.A. Menna, M.C. Cretella, and N.W. Marr
Mobil Solar Energy Corporation
16 Hickory Drive
Waltham, Massachusetts 02254, U.S.A.

ABSTRACT

Primary creep behavior of FZ and CZ silicon between 1200°C and the melting temperature has been studied using four-point bending. Factors investigated were the carbon and oxygen influence, orientation dependence, and temperature and stress level effects on the deformation and on the defect configuration produced. Applied stress levels and times of deformation were chosen to approximate conditions associated with thermal stresses produced in high speed silicon sheet growth.

Defect configurations observed in EFG silicon ribbon grown at speeds of 2 cm/min and above show evidence plastic deformation is produced by thermoclastic stress. Modeling of sheet stress distributions with plastic deformation predicts thermoelastic stresses are significantly reduced by creep in typical EFG growth configurations [1]. At growth rates of 2 to 4 cm/min, thermal stress levels above 1200°C increase to exceed critical yield stresses in times of the order of one minute and less. Primary (transient) creep response then is a dominant factor in determining sheet dislocation and other defect configurations. The strain rate response will further constrain the rate of stress relaxation and limit the regime of growth of low dislocation density and buckle-free sheet.

The transient creep response of low carbon and oxygen ($< 10^{16}$ at/cc) commercial FZ silicon has been compared to CZ silicon with varying levels of substitutional carbon ($1-10 \times 10^{17}$ at/cc) but constant interstitial oxygen of $\sim 1 \times 10^{18}$ at/cc. Strain, strain rates and dislocation densities produced at constant applied stresses in the range of 2-15 MPa are an order of magnitude greater in the FZ than in the CZ silicon. This is attributed to the effects of oxygen on inhibiting dislocation glide and multiplication. Maximum dislocation densities obtained under loading times as short as 5 sec exceed $1 \times 10^7/\text{cm}^2$ in the FZ silicon. The effects of carbon on the transient creep response of the CZ silicon appear to be less pronounced in comparison.

Deformations were carried out at temperatures of 1215°C , 1360°C and 1380°C . Wafers with (111) and (100) surfaces, and respective bending axes of <110> and <100> have been examined. The defect configurations produced in the transient creep experiments are compared to defects observed in the cross section of EFG ribbon, and implications of creep limitations on sheet growth rate are examined.

[1] J.C. Lambropoulos, J.W. Hutchinson, R.O. Bell, B. Chalmers and J.P. Kalejs, J. Crystal Growth, in press.

†This work was supported in part by the Jet Propulsion Laboratory, California Institute of Technology, under Subcontract No. 956312 of the U.S. DOE Flat Plate Solar Array Project.

APPENDIX III

Quarterly Report on Residual Stresses in Sheet Silicon

A. Andonian and S. Danyluk

April 13, 1984

Non-destructive determination of residual stresses in short sections (2 x 4 inch blanks) of EFG sheet has continued this past quarter. Some preliminary results were reported in the previous quarter and the present report summarizes the stress distributions determined by shadow-Moiré interferometry along the growth direction of EFG sheet grown at 2.00 and 2.25 cm/min.

A four-point bend fixture has been constructed and shadow-Moiré interferograms obtained as shown schematically in Fig. 1 [1]. The relative deflection and curvature of the silicon sheet may be obtained from a measurement of the fringe order and density as shown in this figure [2]. These results are then used in a plate analysis to yield the stress distributions. Figure 1 also shows the possible variation of σ_{xx} along the growth direction, and near the ends of the ribbon the σ_{xx} decreases to zero.

Figures 2 and 3 show the σ_{xx} profiles of samples #47R1-2 and 47R1-1 (grown at 2.00 cm/min) at 0.5, 1.0, 2.0, 3.0 and 3.5 in from one end along the growth direction. As can be seen, σ_{xx} is tensile at the center (maximum value of 9 MPa) and compressive at the edges (maximum value of 3 MPa). The stresses are asymmetric relative to the centerline. Figure 4 shows σ_{xx} at the center of sample 47R1-4 grown at 2.25 cm/min. The stress distribution is similar to that shown in the other two figures and expected to be a maximum at this location along the length.

We are continuing to complete the stress analysis along the growth direction of samples #47R1-4 and 47R1-3 (grown at 1.75 cm/min).

[1] Mobil Solar Fourth Quarter Progress Report, DOE/JPL 956312/83/04, August 15, 1983.

[2] C.M. Vest, Holographic Interferometry, John Wiley (1979).

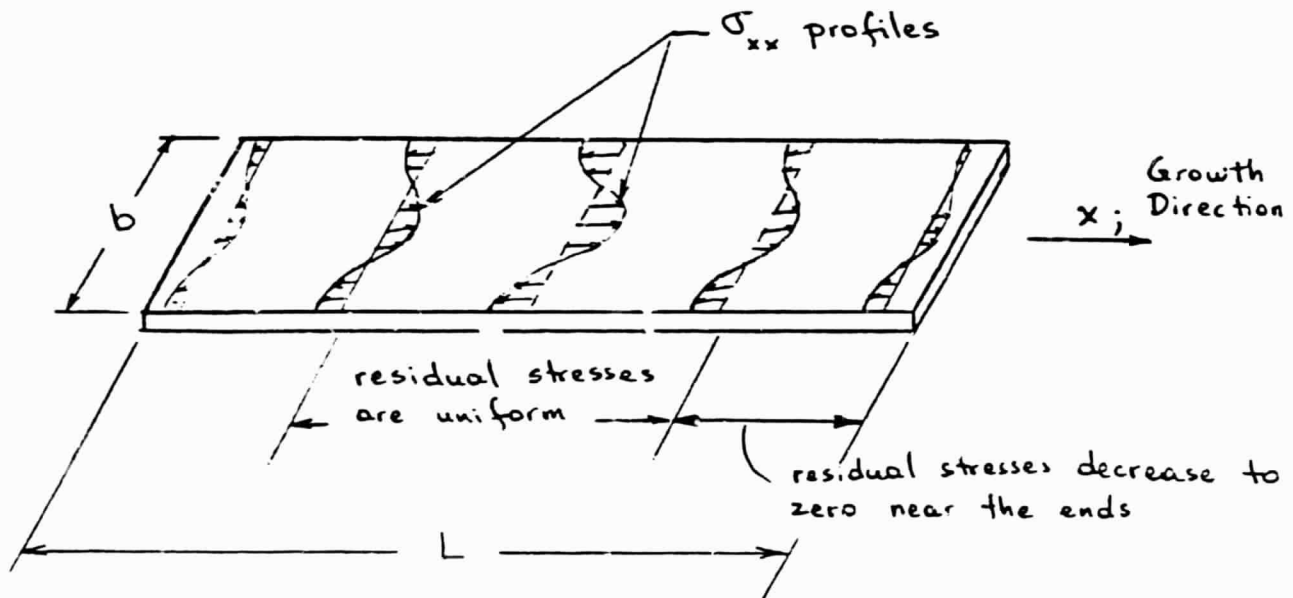
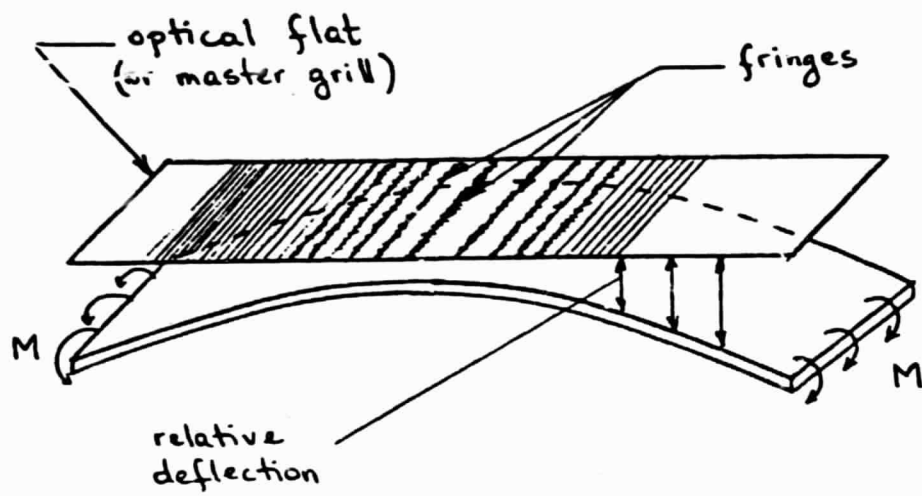


Figure 1

Figure 2. Sample 47R1-2, 2.00 cm/min.

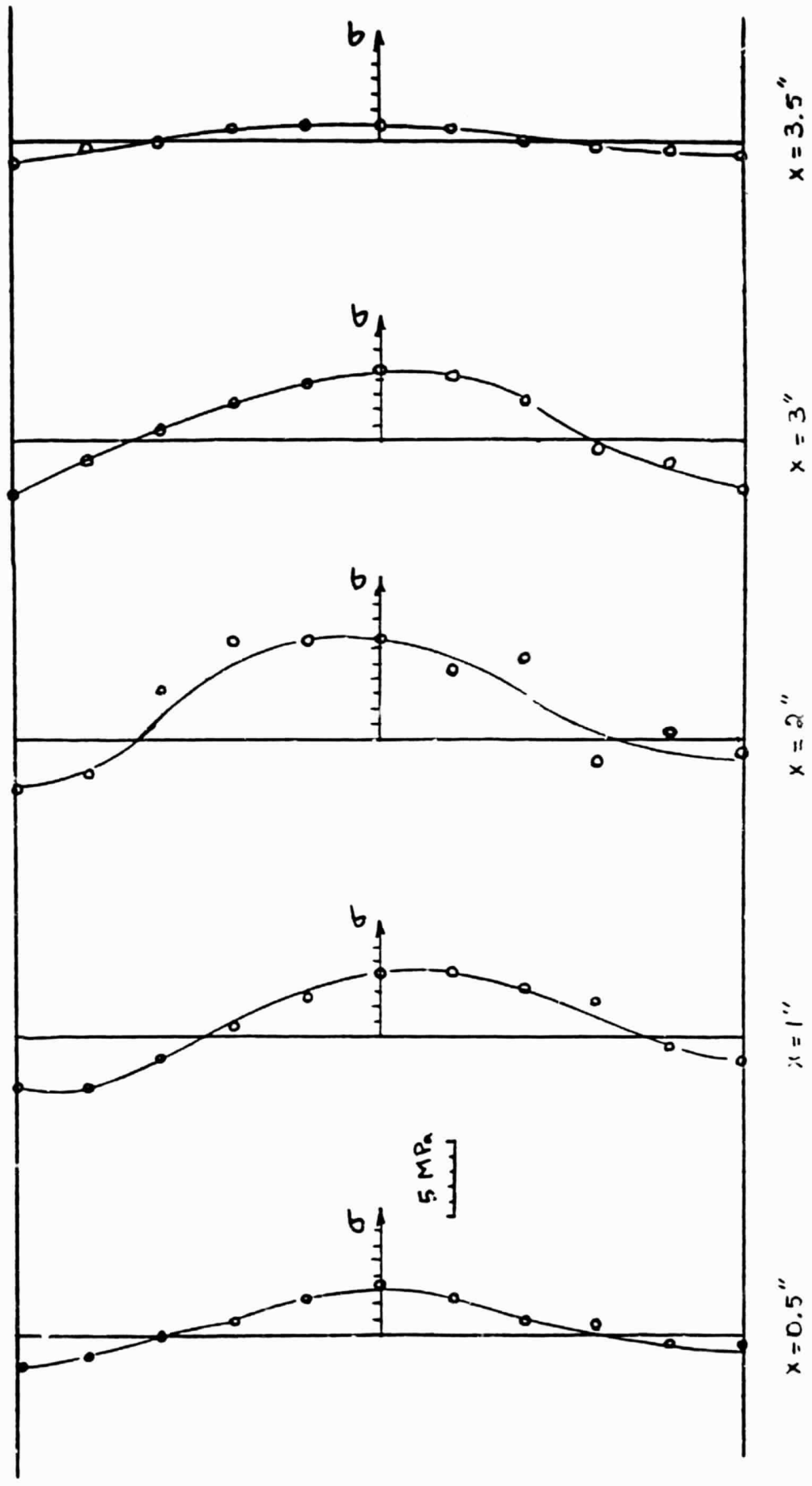


Figure 3. Sample 47R1-1, 2.00 cm/min.

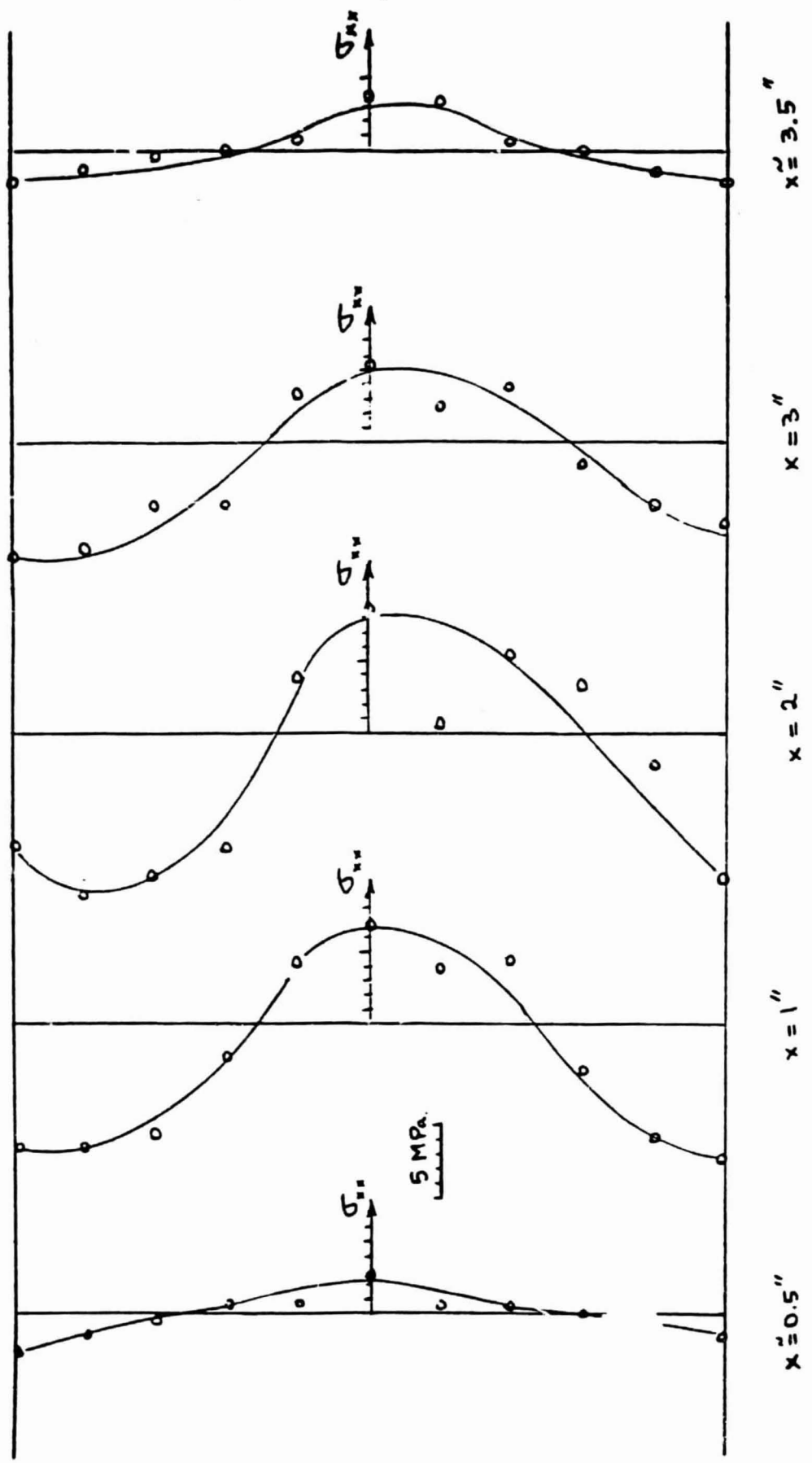
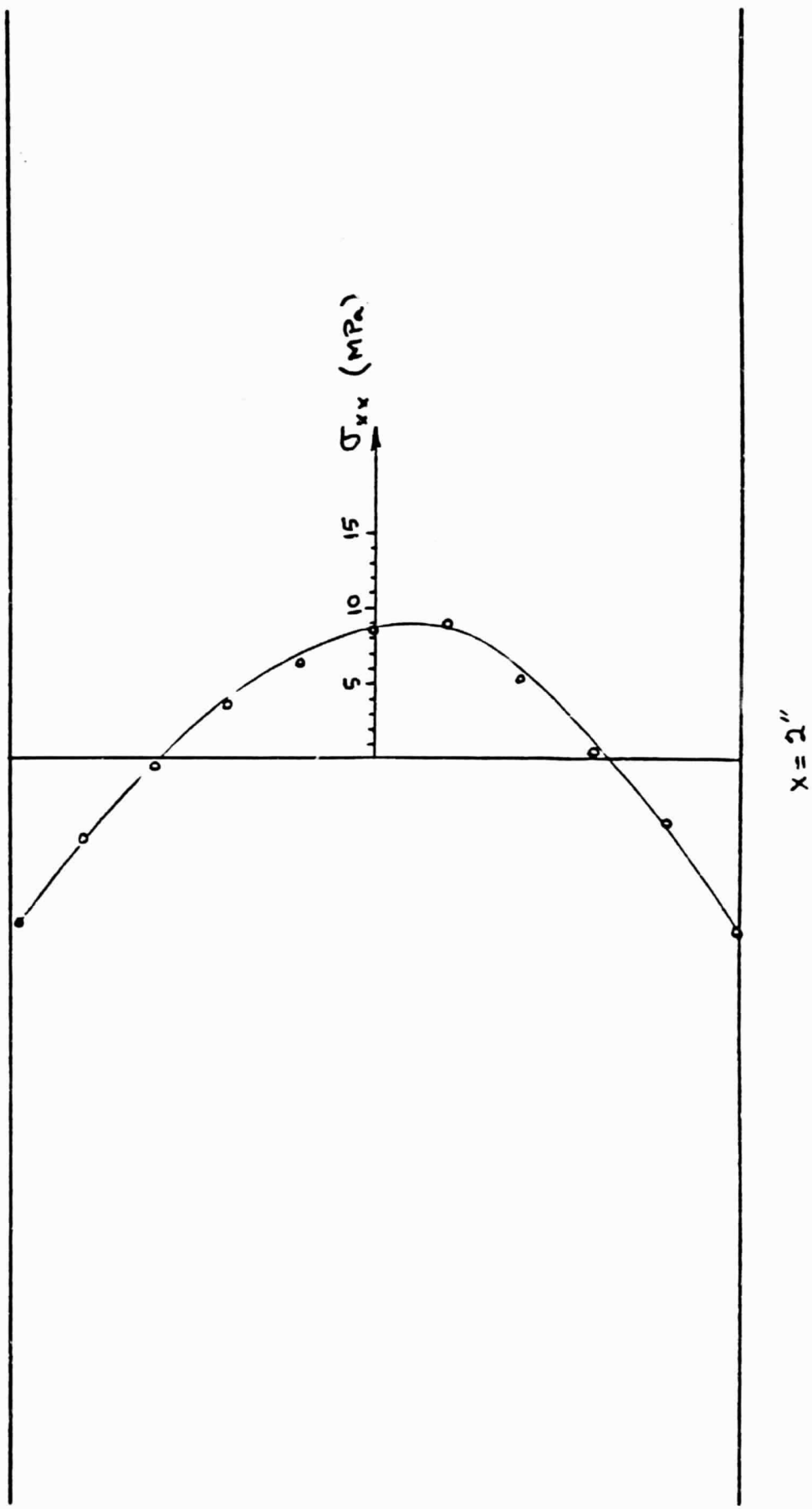


Figure 4. Sample 17R1-4, 2.25 cm/min.



APPENDIX IV
WORK BREAKDOWN STRUCTURE AND PROGRAM PLAN
July 9, 1983 - July 31, 1984
"STRESS STUDIES IN EFG"